

# A single-cell atlas of mouse brain macrophages reveals unique transcriptional identities shaped by ontogeny and tissue environment

Hannah Van Hove<sup>1,2</sup>, Liesbet Martens<sup>3,4</sup>, Isabelle Scheyltjens<sup>1,2</sup>, Karen De Vlaminck<sup>1,2</sup>, Ana Rita Pombo Antunes<sup>1,2</sup>, Sofie De Prijck<sup>4,5</sup>, Niels Vandamme<sup>3,4,6</sup>, Sebastiaan De Schepper<sup>7</sup>, Gert Van Isterdael<sup>4,8</sup>, Charlotte L. Scott<sup>4,5,9</sup>, Jeroen Aerts<sup>10</sup>, Geert Berx<sup>6,11</sup>, Guy E. Boeckxstaens<sup>7</sup>, Roosmarijn E. Vandenbroucke<sup>ID 4,12,13</sup>, Lars Vereecke<sup>13,14,15</sup>, Diederik Moechars<sup>10</sup>, Martin Guilliams<sup>ID 4,5</sup>, Jo A. Van Ginderachter<sup>1,2,17</sup>, Yvan Saey<sup>3,16,17</sup> and Kiavash Movahedi<sup>ID 1,2\*</sup>

While the roles of parenchymal microglia in brain homeostasis and disease are fairly clear, other brain-resident myeloid cells remain less well understood. By dissecting border regions and combining single-cell RNA-sequencing with high-dimensional cytometry, bulk RNA-sequencing, fate-mapping and microscopy, we reveal the diversity of non-parenchymal brain macrophages. Border-associated macrophages (BAMs) residing in the dura mater, subdural meninges and choroid plexus consisted of distinct subsets with tissue-specific transcriptional signatures, and their cellular composition changed during postnatal development. BAMs exhibited a mixed ontogeny, and subsets displayed distinct self-renewal capacity following depletion and repopulation. Single-cell and fate-mapping analysis both suggested that there is a unique microglial subset residing on the apical surface of the choroid plexus epithelium. Finally, gene network analysis and conditional deletion revealed IRF8 as a master regulator that drives the maturation and diversity of brain macrophages. Our results provide a framework for understanding host-macrophage interactions in both the healthy and diseased brain.

The brain is a compartmentalized organ that contains diverse border regions which form the interface with the periphery. Each of these borders is associated with its own degree of steady-state ‘immune privilege’ due to the presence of distinct endothelial and epithelial barriers<sup>1,2</sup>. The brain parenchyma is covered by the three-layered meninges. The upper dural layer constitutes a more permissive border due to the presence of fenestrated blood vessels and lymphatics<sup>3–6</sup>. In contrast to the dural vessels, the vasculature in the subdural meninges contains tight junctions forming the blood-leptomeningeal barrier. The perivascular space around the parenchymal vasculature also forms a border region with low accessibility due to the presence of the blood-brain barrier<sup>2</sup>. Finally, the choroid plexus (CP), which floats in the brain’s ventricles, contains fenestrated blood vessels that form a dense network embedded in the CP stroma<sup>1,2,7</sup>. This loose connective tissue is lined by a single layer of CP epithelial cells that are interconnected with tight junctions and form the blood-cerebrospinal fluid (CSF) barrier. The brain has recently been shown to contain a heterogeneous immune

compartment, with most of the diversity thought to be restricted to its border regions<sup>8–10</sup>.

Macrophages are professional phagocytes that are integral to innate immune defense but are also now emerging as critical regulators of tissue homeostasis<sup>11</sup>. A clear example of a macrophage population that plays an instrumental role in tissue homeostasis is that of microglia. Homeostatic microglia are highly dynamic cells that continuously survey neuronal synapses and contribute to activity-dependent refinement of neural circuits via synaptic pruning<sup>12</sup>. Microglia are also key actors in neuroinflammatory and neurodegenerative diseases<sup>12</sup>. While the critical role of microglia in brain homeostasis and disease is gradually being uncovered, much less is known about other tissue-resident macrophages of the brain residing at its borders. Indeed, border-associated macrophages (BAMs) can be found in the perivascular space, meninges and CP where, besides stromal macrophages, the CP epithelium also contains an uncharacterized macrophage-like population called Kolmer’s epi-plexus cells<sup>8,12–14</sup>. In the perivascular space and subdural meninges,

<sup>1</sup>Myeloid Cell Immunology Lab, VIB Center for Inflammation Research, Brussels, Belgium. <sup>2</sup>Lab of Cellular and Molecular Immunology, Vrije Universiteit Brussel, Brussels, Belgium. <sup>3</sup>Data Mining and Modeling for Biomedicine, VIB Center for Inflammation Research, Ghent, Belgium. <sup>4</sup>Department of Biomedical Molecular Biology, Ghent University, Ghent, Belgium. <sup>5</sup>Laboratory of Myeloid Cell Ontogeny and Functional Specialization, VIB Center for Inflammation Research, Ghent, Belgium. <sup>6</sup>Cancer Research Institute Ghent, Ghent, Belgium. <sup>7</sup>Department of Chronic Diseases, Metabolism and Ageing, Translational Research Center for Gastrointestinal Disorders, Center of Intestinal Neuro-immune Interactions, KU Leuven, Leuven, Belgium. <sup>8</sup>VIB Flow Core, VIB Center for Inflammation Research, Ghent, Belgium. <sup>9</sup>Institute of Infection, Immunity and Inflammation, College of Medical, Veterinary and Life Sciences, University of Glasgow, Glasgow, UK. <sup>10</sup>Department of Neuroscience, Janssen Research & Development (a division of Janssen Pharmaceutica NV), Beerse, Belgium. <sup>11</sup>Molecular and Cellular Oncology Laboratory, Department of Biomedical Molecular Biology, Ghent University, Ghent, Belgium. <sup>12</sup>Barriers in Inflammation lab, VIB Center for Inflammation Research, Ghent, Belgium. <sup>13</sup>Ghent Gut Inflammation Group, Ghent University, Ghent, Belgium.

<sup>14</sup>Host-Microbiota Interaction lab, VIB Center for Inflammation Research, Ghent, Belgium. <sup>15</sup>Department of Rheumatology, University Hospital Ghent, Ghent, Belgium. <sup>16</sup>Department of Applied Mathematics, Computer Science and Statistics, Ghent University, Ghent, Belgium. <sup>17</sup>These authors contributed equally: Jo A. Van Ginderachter, Yvan Saey. \*e-mail: [kiavash.movahedi@vub.vib.be](mailto:kiavash.movahedi@vub.vib.be)

BAMs have an embryonic origin while CP BAMs exhibit a mixed ontogeny<sup>13</sup>. The ontogeny of dural BAMs is unclear and it is not known whether stromal CP macrophages and Kolmer's epiplexus cells share a similar ontogeny.

To uncover the full immune diversity at the brain's borders, together with a detailed analysis of its macrophage populations, we isolated brains or individual border regions from homeostatic, diseased or gene-targeted mice and employed droplet-based, single-cell RNA-sequencing (scRNA-seq) combined with complementary approaches. This yielded extensive insights into the immune cell diversity at the brain's borders and revealed the tissue-specific signatures of BAMs, including the identification of a microglial-like subset lining the apical surface of the CP epithelium. To facilitate the use of our scRNA-seq datasets, we have also developed a straightforward online tool for evaluating gene expression at single-cell resolution ([www.brainimmuneatlas.org](http://www.brainimmuneatlas.org)).

## Results

**Unraveling regional immune cell heterogeneity in the brain via scRNA-seq of discrete brain compartments.** To obtain a comprehensive understanding of immune cell heterogeneity in the homeostatic brain, we isolated whole mouse brains or micro-dissected border regions and performed scRNA-seq on sorted CD45<sup>+</sup> cells (Fig. 1a). Since we were unable to peel off the pia/arachnoid mater from the parenchyma, thin slices were collected from the dorsal surface of the brain to enrich for the subdural meninges (SDM). Unsupervised clustering and *t*-distributed stochastic neighbour-embedding (tSNE) projections were performed on 6,530 cells from whole brain (Fig. 1b), on 6,564 cells from enriched SD meninges (Fig. 1c), on 5,865 cells from the dura mater (Fig. 1d) and on 3,940 cells from the CP (Fig. 1e). Cells from the various brain regions were also pooled into a single dataset (Fig. 1f) and the origin of each cell was visualized in a color-coded tSNE plot (Fig. 1g). Clusters were identified based on the expression of known marker genes (Fig. 1h and Supplementary Table 1). The majority of immune cells in homeostatic brains were microglia (Fig. 1b). The brain also contained various lymphocyte populations, present in varying percentages in the distinct brain regions (Fig. 1b–h). The brain and, in particular, its borders contained a large and heterogeneous myeloid compartment, which was investigated in more depth.

Dendritic cells (DCs) were detected in all samples but were most prevalent in the dura mater, where multiple subsets were found (Fig. 1d,i). We identified plasmacytoid DCs (pDCs, *Siglech*<sup>+</sup> *Ccr9*<sup>+</sup> *Pacsin1*<sup>+</sup>) and conventional DCs (cDCs) that could be further subdivided into the subsets cDC1 (*Flt3*<sup>+</sup> *Irf8*<sup>hi</sup> *Xcr1*<sup>+</sup>) and cDC2 (*Flt3*<sup>+</sup> *Irf8*<sup>lo</sup> *Cd209*<sup>+</sup>)<sup>15</sup> (Fig. 1i). cDCs expressed *Zbtb46*, which was absent/low on pDCs and monocytes/macrophages as described previously<sup>16</sup>. Remarkably, in the dura and CP we also observed a DC cluster with a gene signature reminiscent of migratory DCs<sup>16</sup> (migDCs) (Fig. 1d, cluster 8), including the expression of *Ccr7* and *Nudt17*. This suggests that the brain's borders contain migDCs that may migrate to draining lymph nodes. The ratios of the various DC subsets differed in the distinct border regions: meninges contained more cDC2s while cDC1s were predominant in the CP (Fig. 1j). pDCs were restricted to the dura.

The dura mater contained the highest percentage of monocytes, including both classical and non-classical subsets<sup>17</sup> and an intermediate monocyte/macrophage population termed monocyte-derived cells (MdCs) (Fig. 1d). Macrophages that were distinct from microglia were observed in the whole-brain sample and were detected in large numbers in the dissected border regions (light coral clusters in Fig. 1b–e). These BAMs<sup>8</sup> were identified based on a high expression of prototypical macrophage genes (for example, *Adgre1*, *Fcgr1*, *Aif1*) and a low expression of monocyte and cDC genes (see dot plots in Fig. 1c–e). While we expect that the majority of BAMs in the enriched SDM sample represented pia/arachnoid macrophages,

some may have been perivascular macrophages derived from the thin cortical region underneath the pia mater, which also contained 'contaminating' microglia (Fig. 1c).

In the CP, substantial heterogeneity was observed at the level of immediate early genes (IEGs). The CP-BAMA population was split into two major clusters (CP-BAM A1 and CP-BAM A2; Supplementary Fig. 1a,b), due to the differential expression of IEGs (Supplementary Fig. 1c). A probable explanation is dissociation-induced IEG induction<sup>18,19</sup> in part of the population. Since dissociation-induced IEGs could have masked the inherent heterogeneity of CP-BAMs, this source of variation was regressed out of the data (Supplementary Fig. 1a,d,e). However, to ascertain whether differential IEG expression was dissociation induced and not present in vivo, we implemented the Act-Seq strategy<sup>20</sup>. A side-by-side comparison was made of dura mater and CP samples that were isolated and processed either using our standard procedure or by implementing Act-Seq modifications, which included the addition of the transcription inhibitor actinomycin D (ActD) (Supplementary Fig. 2a). Remarkably, cells from all clusters showed some level of segregation when comparing the two isolation procedures, in both the dura (Supplementary Fig. 2b) and CP (Supplementary Fig. 2e), which was the result of a reduction in IEG expression in the ActD samples (Supplementary Fig. 2c,d,f,g). When comparing standard and ActD BAMs in the dura or CP, IEGs were strongly upregulated (Supplementary Fig. 2d,g). These were the same genes that were differential between CP-BAM A1 and CP-BAM A2 (Supplementary Fig. 1c), confirming that the expression of these genes was dissociation induced.

**Border-associated macrophages are highly heterogeneous and exhibit tissue-specific transcriptional signatures.** To further characterize BAM heterogeneity and potential tissue-specific signatures, microglia and BAMs from the whole brain or distinct border regions were re-analysed in a single dataset (Fig. 2a). This revealed six major BAM subsets that clustered separately from microglia (Fig. 2a,b). Cluster SD-BAM consisted mainly of subdural macrophages. Dural macrophages were split into two major subsets: D<sup>lo</sup>-BAMs and D<sup>hi</sup>-BAMs (referring to low and high MHCII expression, respectively). A small subset of subdural macrophages co-clustered with dural macrophages in D<sup>hi</sup>-BAM. CP macrophages clustered separately from meningeal macrophages, and most were found in clusters CP<sup>lo</sup>-BAM and CP<sup>hi</sup>-BAM. Remarkably, a small subset of CP macrophages (representing cluster CP-BAM B in Fig. 1e) clustered separately from other BAMs or microglia (CP<sup>epi</sup>-BAM).

Next, we examined the expression of previously reported microglial signature genes<sup>21,22</sup> in the various BAM subsets (Fig. 2c). While these signature genes were highly expressed in microglia, many were co-expressed to some degree in BAMs. Genes that were highly restricted to microglia included *Sall1* and *Sparc*. Interestingly, in contrast to the other BAM subsets, CP<sup>epi</sup>-BAMs also expressed all microglial signature genes, albeit often at lower levels. This suggests that while these CP macrophages were not identical to parenchymal microglia, they may have a shared ontogeny or phenotype.

BAMs exhibited distinct transcriptional states and we identified sets of signature genes that were either shared between the various BAM subsets or were unique for a specific population (Fig. 2d,e). Universal BAM signature genes included *Apoe*, *Ms4a7*, *Ms4a6c*, *Lyz2* and *Tgfb1*. Most of these genes were absent or sparse in CP<sup>epi</sup>-BAMs, which more closely resembled the expression pattern of microglia. Furthermore, BAMs fell into two main groups: MHCII<sup>lo</sup> and MHCII<sup>hi</sup>, which exhibited many differentially expressed genes (for example, *Mrc1*, *Cd163*, *Gas6* versus *H2-Aa*, *Cd74*, *Klra2*). BAMs also exhibited clear tissue-specific signatures. Signature genes were identified that specifically marked meningeal MHCII<sup>lo</sup> BAMs (for example, *Clec4n*, *Clec10a*, *Folr2*) or were enriched in SD-BAMs (for example, *Lyve1*, *P2rx7*, *Egfl7*), individual dural BAM subsets

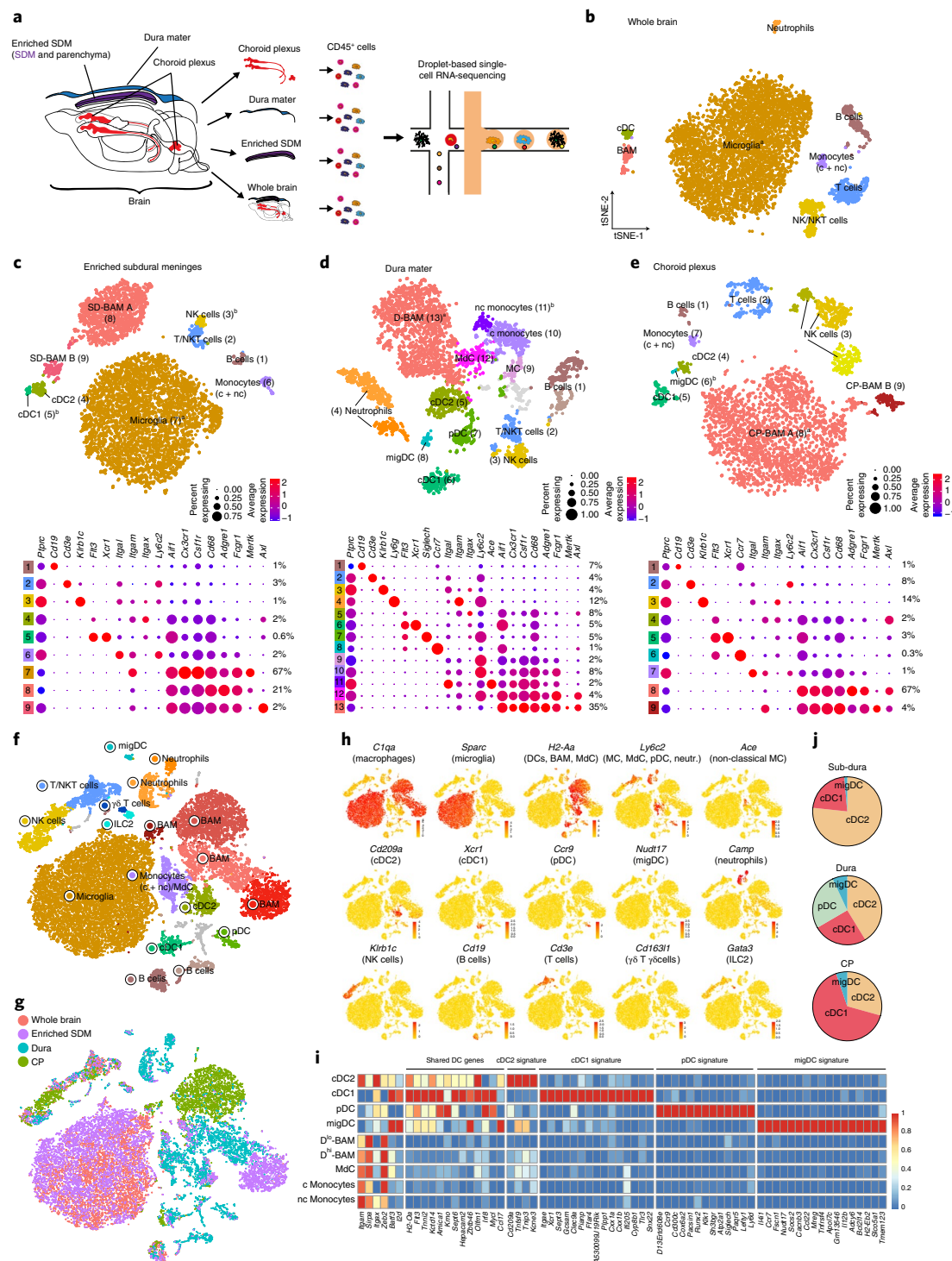


**Fig. 1 | scRNA-seq of discrete brain compartments reveals regional immune cell heterogeneity.** **a**, Schematic overview of the 10X chromium scRNA-seq procedure used on CD45<sup>+</sup> immune cells isolated from the whole brain and microdissected border regions of 9-week-old C57BL/6 mice. **b**, tSNE plot of 6,530 cells isolated from the whole brain, showing the immune cell populations that were identified via unsupervised clustering. **c–e**, tSNE plot of 6,654 cells isolated from the enriched SD meninges (SDM). **d**, tSNE plot of 5,865 cells isolated from the dura mater. **e**, tSNE plot of 3,940 cells isolated from the CP (following regress out of IEGs; see Supplementary Fig. 1). **c–e**, Dot plots corresponding to tSNE plots of the border regions showing the expression of subset-specific genes, with the dot size representing the percentage of cells expressing the gene and the color representing its average expression within a cluster. The percentage of each cluster within the total population is given on the right-hand side of each dot plot. **f**, tSNE plot of 21,966 CD45<sup>+</sup> cells pooled from the whole brain and border regions. **g**, Similar to **f** but with the colors representing the tissue origin of cells. **h**, tSNE maps showing the expression of key marker genes for the indicated immune cell populations. The color code (gold, low expression; red, high expression) and range of log<sub>2</sub> normalized counts are shown at lower right on each plot. **i**, Heatmap of normalized expression for selected genes in DC subsets and other indicated populations in the dura mater. **j**, Pie charts showing the proportions of different DC subsets within each border region (SDM, dura mater and CP). <sup>a</sup>Sub-clusters within the macrophage populations are omitted for clarity. <sup>b</sup>Cluster was manually selected. NK/NKT cells, natural killer/natural killer T cells; c, classical monocyte; nc, non-classical monocyte; Mdc, monocyte-derived cell; MC, monocytic cell; ILC, innate lymphoid cell.

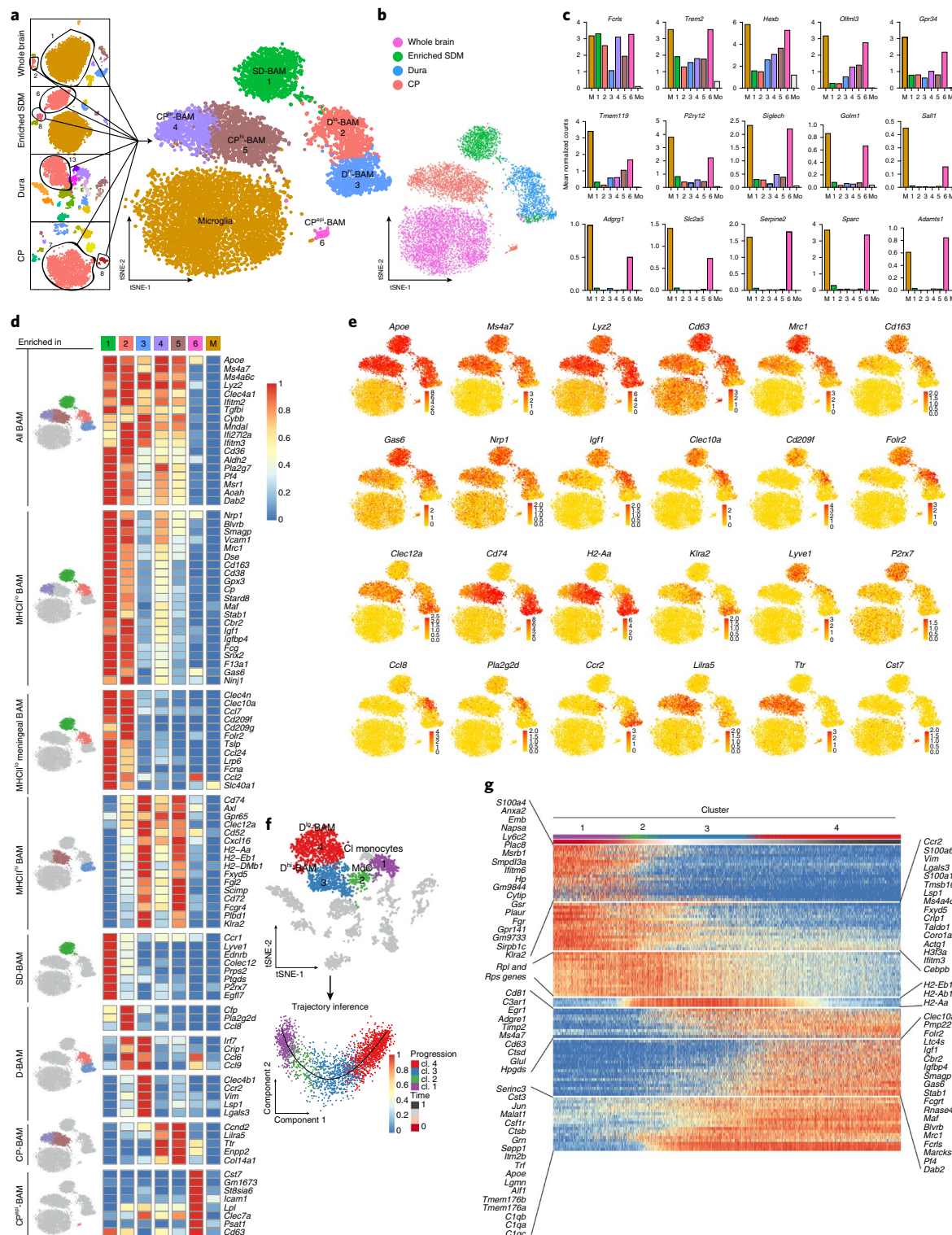


**Fig. 2 | Border-associated macrophages are heterogeneous and exhibit tissue-specific transcriptional signatures. a,** tSNE plot of 10,947 macrophages pooled from the whole brain and border regions revealing the existence of six BAM subsets. **b,** Similar to a but with the colors representing the tissue origin of cells. **c,** Bar plots showing the mean log<sub>2</sub> normalized counts of previously reported microglial signature genes in microglia and the BAM subsets that were identified in a. Gene expression levels in classical monocytes (Mo) from the dura mater are included as an additional reference. M, microglia. **d,** Heatmap of normalized gene expression in microglia and the BAM subsets that were identified in a. Genes are grouped based on their signature expression in the indicated BAM subsets. **e,** tSNE maps showing the expression of various BAM signature genes. **f,** SCORPIUS trajectory inference on classical monocytes, MDCs and BAMs from the dura mater. Cells were automatically ordered along a linear trajectory as shown. **g,** The top 100 genes were clustered into seven gene modules (normalized expression) that correspond to the transition from monocytes to BAMs.

(for example, *Pla2g2d*, *Ccl8*) or CP BAMs (for example, *Lilra5*, *Ttr*). CP<sup>epi</sup>-BAMs also exhibited a unique transcriptional profile, which included expression of *Cst7*, *Gm1673* and *Clec7a*.

A graded expression of monocyte genes, such as *Ccr2*, was observed in MHCII<sup>hi</sup> BAMs, suggesting a monocytic origin. When performing SCORPIUS trajectory inference<sup>23</sup> on monocytes, MdCs and BAMs from the dura, these cells were ordered along a linear trajectory (Fig. 2f). The most predictive genes were clustered into modules, which showed transcriptional gradients of genes that were lost or gained as cells moved from a monocytic state to mature BAMs (Fig. 2g).

**BAM subsets can be identified at the protein level via high-dimensional fluorescence cytometry.** To correlate single-cell gene and single-cell protein expression, we employed high-dimensional fluorescence cytometry. Based on our scRNA-seq data, we devised two antibody panels: a general myeloid-centered panel and a macrophage-centered panel to differentiate between the various BAM subsets (Fig. 3a). Flow cytometry was performed on the whole brain or dissected border regions followed by tSNE analysis. Using the general panel, all major myeloid subsets could be identified and a manual gating strategy was devised for selection of microglia, BAM subsets, cDCs, monocytes/MdCs and other myeloid cells (Supplementary Fig. 3a–c), which was mapped onto the tSNE plots (Fig. 3b). The various BAM subsets could also be identified using more restricted seven-color panels (Supplementary Fig. 3d). However, these panels did not allow distinction among BAM subsets originating from the different border regions in whole-brain samples. Therefore, we first verified the protein expression of subset-specific signature genes via flow cytometry (Supplementary Fig. 4), which was then used to design a flow panel and gating strategy to identify all BAM subsets in dissected or whole-brain samples (Fig. 3c). When pooling macrophages from different border regions in a single dataset with corresponding tSNE plots, BAMs from the different borders clustered separately from each other and from microglia (Fig. 3d) and a good overlap was seen with the overlaying manual gates (Fig. 3e). Key signature markers used for BAM identification were P2RX7, MMR (CD206), FOLR2, NRP1, CD63, MHCII, CLEC12A and CD45 (Fig. 3f).

The tissue-specific adaptation of BAMs from different border regions was also reflected at the level of their morphology. To visualize this, we relied on wholemount immunostaining which exposed the clearly distinct morphologies of subdural and dural BAMs (Fig. 3g–j). To confirm that the examined populations were resident macrophages, we relied on cell tracing in *Cx3cr1*<sup>CreER</sup>:R26-YFP mice

in which, four weeks after tamoxifen injection, only resident macrophages remained YFP-labeled in the brain<sup>24</sup>.

**Bulk RNA-seq of BAM subsets further uncovers their transcriptional state and suggests tissue-specific functional adaptations.** To complement our scRNA-seq results we sorted BAMs for bulk RNA-seq, which allows for more in-depth profiling. To assess inter-border variation, we compared C<sup>hi</sup>-BAMs and D<sup>hi</sup>-BAMs (Fig. 4a). For intra-border heterogeneity, D<sup>hi</sup>-BAMs were compared to D<sup>lo</sup>-BAMs. Microglia were included as a reference population. To further unveil BAM-specific gene signatures, we included tissue-resident macrophages from peritoneum, lung and liver (Fig. 4a). Principal component analysis of gene expression showed that while brain macrophages exhibited subset-specific segregation, they clustered closer together and at greater distances from peripheral macrophages (Fig. 4b). This was confirmed by Pearson correlation coefficients (Fig. 4c). Hundreds of DE genes were observed when comparing brain and peripheral macrophages (Fig. 4d). Microglia showed the highest number of uniquely upregulated genes ( $n=865$ ), followed by C<sup>hi</sup>-BAMs ( $n=275$ ). Many significantly upregulated genes ( $n=706$ ) were shared among all brain macrophage subsets. From these DE gene lists, we constructed heatmaps to reveal the signature gene expression of brain macrophages (Supplementary Fig. 5a,b).

A total of 1,295 DE genes were observed between C<sup>hi</sup>- and D<sup>hi</sup>-BAMs (Fig. 4e). This confirms that BAMs from different border regions possess unique transcriptional profiles. D<sup>hi</sup>-BAMs and D<sup>lo</sup>-BAMs were more similar, but still exhibited 541 DE genes (Fig. 4f). To investigate how the transcriptional diversity of BAMs may relate to their functions, we used the DE genes between BAMs and microglia to construct gene ontology networks. Microglia-enriched genes were related to functions such as neurogenesis and TGF- $\beta$  signaling (Supplementary Fig. 5c), while universally upregulated BAM genes were linked to blood vessel development, lipid and cholesterol metabolism, immune response and antigen presentation (Fig. 4g). Genes that were restricted to one or two BAM subsets revealed subset-specific gene ontologies (Fig. 4h), including categories related to angiogenesis, ion transport and cell migration.

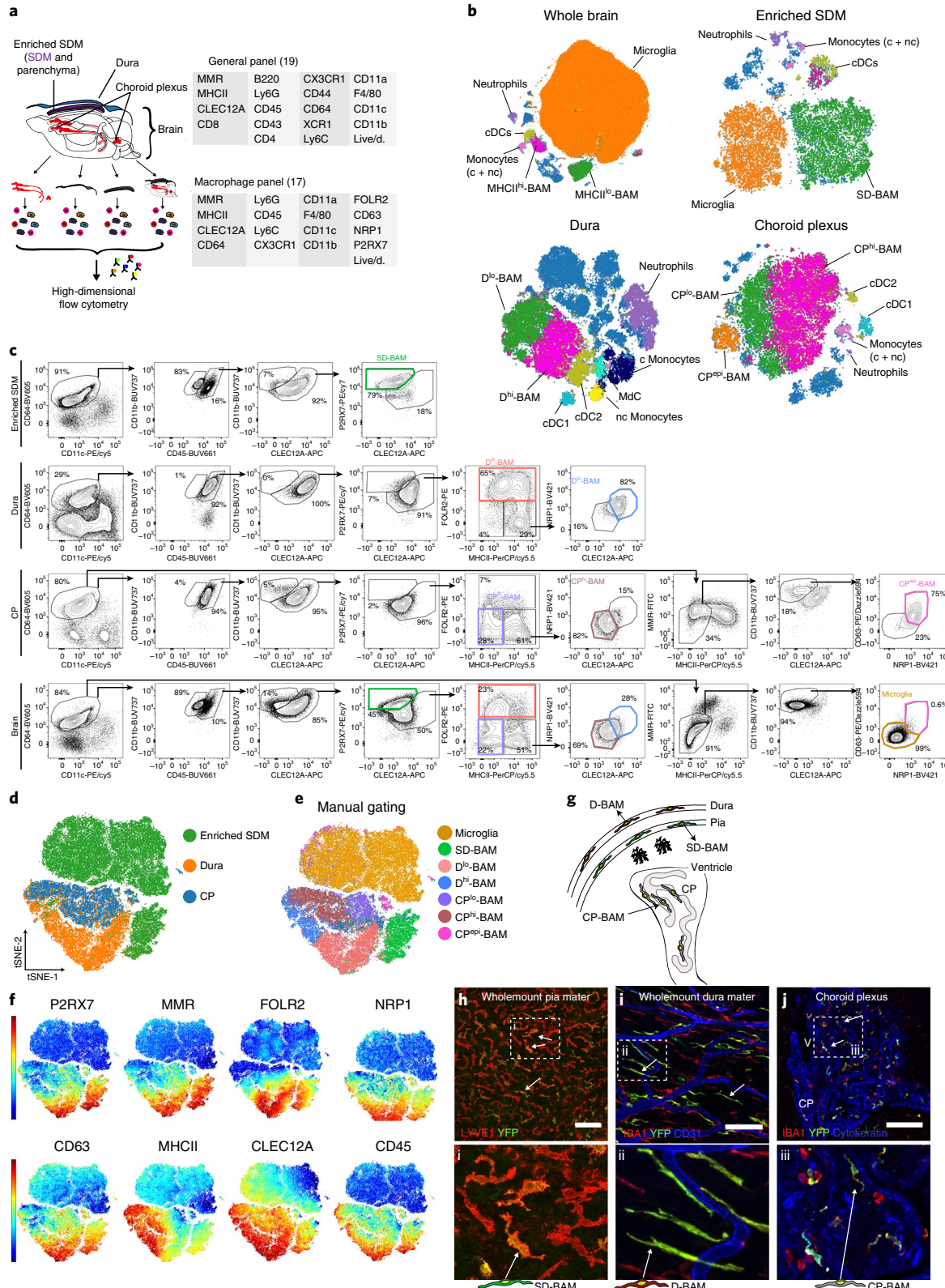
**Sall1<sup>+</sup> CP<sup>epi</sup>-BAMs reside on the apical surface of the CP epithelium.** Since CP<sup>epi</sup>-BAMs expressed *Sall1* (Fig. 2c), we used *Sall1*<sup>CreER</sup>:R26-YFP mice to trace these cells in the CP. Tamoxifen injections in *Sall1*<sup>CreER</sup> mice efficiently labeled parenchymal microglia (Fig. 5a,b). Interestingly, we also observed a YFP<sup>+</sup> BAM subset in the lateral ( $5.6\% \pm 0.9\%$ ) and fourth ventricles of the CP ( $2.6\% \pm 0.5\%$ ) (Fig. 5a,b). *Sall1*<sup>+</sup> CP-BAMs were

**Fig. 3 | Identification of BAM subsets using high-dimensional fluorescence cytometry.** **a**, Single cells from the whole brain and border tissues of 9-week-old C57BL/6 mice were stained with two antibody panels for fluorescence cytometry on FACSymphony: a general 19-color antibody panel and a macrophage-specific 17-color antibody panel. **b**, General panel: manually gated myeloid populations (Supplementary Fig. 3c) were mapped onto the tSNE plot of the whole brain, enriched SDM, dura and CP. **c**, classical monocyte; nc, non-classical monocyte. Blue represents ungated cells. Representative of three independent experiments. **d–f**, Macrophage panel. **c**, Representative flow cytometry plots depicting the identification of microglia and BAM subsets in the dissected border regions and whole brain. Cells were pre-gated as CD45<sup>+</sup> live single cells. BAMs were gated as CD64<sup>hi</sup>CD11c<sup>lo</sup>CD11b<sup>hi</sup>CD45<sup>int</sup>CLEC12A<sup>+</sup> cells. SD-BAMs (green) were P2RX7<sup>hi</sup>CLEC12A<sup>int</sup>, while D-BAMs and CP-BAMs were P2RX7<sup>lo-int</sup>CLEC12A<sup>int-hi</sup> cells. D<sup>lo</sup>-BAMs (red) were FOLR2<sup>hi</sup> and further gated as NRP1<sup>hi</sup>CLEC12A<sup>hi</sup> (not shown). D<sup>hi</sup>-BAMs (blue) were FOLR2<sup>lo</sup>MHCII<sup>hi</sup>NRP1<sup>hi</sup>CLEC12A<sup>hi</sup>. CP<sup>lo</sup>-BAMs (purple) were gated as FOLR2<sup>lo</sup>MHCII<sup>lo</sup>, and CP<sup>hi</sup>-BAMs (brown) as FOLR2<sup>lo</sup>MHCII<sup>hi</sup>NRP1<sup>lo</sup>CLEC12A<sup>int</sup>. Microglia and CP<sup>epi</sup>-BAMs were gated as CD64<sup>hi</sup>CD11c<sup>lo</sup>MMR<sup>lo</sup>MHCII<sup>lo</sup>CD11b<sup>hi</sup>CLEC12A<sup>lo</sup> cells. Microglia (gold) were NRP1<sup>lo</sup>CD63<sup>lo</sup>, while CP<sup>epi</sup>-BAMs (pink) were NRP1<sup>int</sup>CD63<sup>hi</sup>. **d**, tSNE plot from BAMs and microglia pooled from the dissected border regions. Macrophages were pre-gated as CD45<sup>+</sup>CD11b<sup>hi</sup>CD64<sup>hi</sup>Ly6C<sup>lo</sup>CD11c<sup>lo</sup> live single cells. Colors correspond to the tissue origin of the cells. **e**, Manually gated BAM populations and microglia were mapped onto the tSNE plot of the pooled BAMs and microglia from the dissected border regions. **f**, tSNE plots from the pooled BAMs and microglia from the dissected border regions showing the expression of key marker genes. Results in **c–f** are representative of three independent experiments. **g**, Legend corresponding to **h–j** showing in situ location of the different BAM subsets (red, D-BAMs; green, SD-BAMs; gray, CP-BAMs). **h–j**, Wholemount of pia mater (**h**), wholemount of dura mater (**i**) and coronal section of the lateral ventricle CP (**j**) from tamoxifen-treated *Cx3cr1*<sup>CreER</sup>:R26-YFP mice, following a 4-week washout period. SD-BAMs were identified as LYVE1<sup>+</sup>YFP<sup>+</sup> cells in **h**, while dural and CP-BAMs were identified as IBA1<sup>+</sup> YFP<sup>+</sup> cells in **i** and **j**, respectively. Dural blood vessels and CP epithelium were stained with anti-CD31 and anti-cytokeratin, respectively. Representative images of  $n=3$  (**h**), 4 (**i**) and 2 (**j**) mice. Scale bars, 100  $\mu$ m.

MHCII<sup>+</sup>-CLEC12A<sup>−</sup> and exhibited higher CD11b staining than *Sall1*<sup>+</sup> CP-BAMs (Fig. 5c).

To investigate the spatial distribution of *Sall1*<sup>+</sup> CP-BAMs, we performed immunostaining in *Sall1*<sup>CreER</sup>;R26-YFP mice. YFP expression was observed in a fraction of IBA1<sup>+</sup> CP macrophages, confirming *in situ* that the CP contains a *Sall1*<sup>+</sup> BAM subset

(Fig. 5d,e). Interestingly, YFP<sup>+</sup>IBA1<sup>+</sup> BAMs were observed only on the apical surface of the cytokeratin-stained CP epithelium while stromal IBA1<sup>+</sup> macrophages were YFP<sup>−</sup>. In contrast to YFP<sup>−</sup> BAMs, YFP<sup>+</sup> BAMs did not exhibit CLEC12A staining (Fig. 5f). Additionally, apical IBA1<sup>+</sup> cells exhibited lower *Lyz2*<sup>GFP</sup> expression compared to stromal BAMs (Fig. 5g), in line with scRNA-seq data



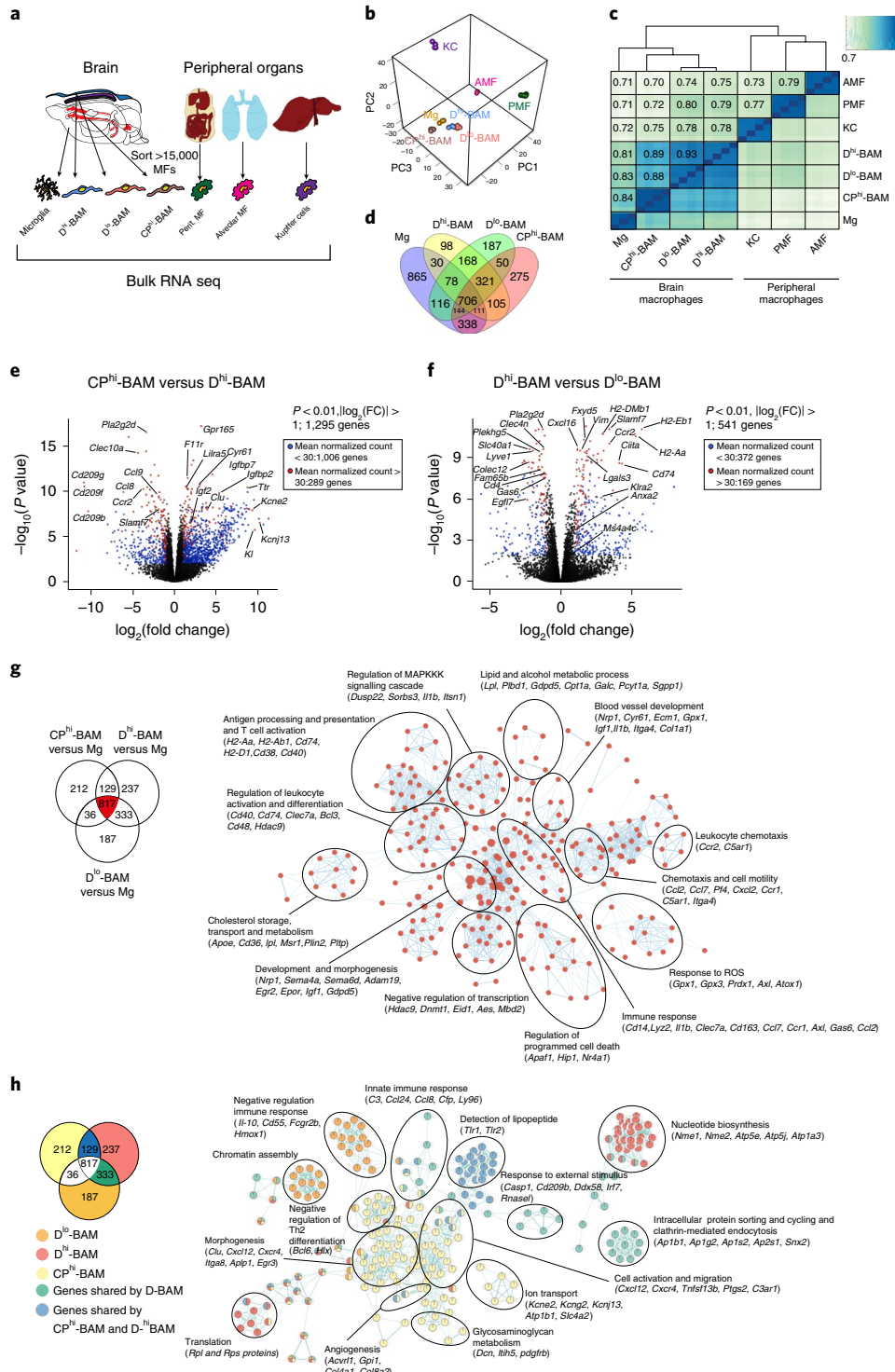


**Fig. 4 | Bulk RNA-seq of BAM subsets suggests tissue-specific functional adaptations.** **a**, Schematic overview of bulk RNA-seq performed on various brain and peripheral macrophages. MF, macrophage; Mg, microglia; PMF, peritoneal macrophage; AMF, alveolar macrophage; KC, Kupffer cell. **b**, Principal component analysis of gene expression for brain and peripheral macrophage populations. **c**, Pearson correlation matrix of brain and peripheral macrophages based on gene expression. **d**, Genes that were significantly upregulated in microglia or BAM subsets as compared to all three peripheral macrophages (PMFs, AMFs, KCs) are shown in the Venn diagram (adjusted  $P < 0.01, \log_2(\text{FC}) > 1$ );  $P$  values were corrected for multiple testing by the Benjamini–Hochberg method. **e,f**, Volcano plots displaying genes that are DE (adjusted  $P < 0.01, \log_2(\text{FC}) > 1$ ) between (**e**) CP<sup>hi</sup>-BAMs versus D<sup>hi</sup>-BAMs and (**f**) D<sup>hi</sup>-BAMs versus D<sup>lo</sup>-BAMs. Blue dots represent DE genes with mean normalized count < 30; red dots represent DE genes with mean normalized count > 30.  $P$  values were corrected for multiple testing by the Benjamini–Hochberg method. **b–f**,  $n = 4$  (or 3 for microglia) independent sorts per macrophage subset. **g,h**, Gene ontology network based on genes that are DE between BAM subsets versus microglia. The Venn diagram displays unique and intersecting DE genes among the different BAM subsets. Each node represents a gene ontology. A selection of genes associated with each cluster of gene ontologies is displayed. Gene ontology network based on DE genes shared by all BAM subsets with  $\log_2(\text{FC}) > 1$  (**g**) and based on DE genes unique to CP<sup>hi</sup>-BAMs (yellow), D<sup>hi</sup>-BAMs (red), D<sup>lo</sup>-BAMs (orange), shared by D-BAMs (green) and shared by CP<sup>hi</sup>- and D<sup>hi</sup>-BAMs (blue) with  $\log_2(\text{FC}) > 1$  (**h**).

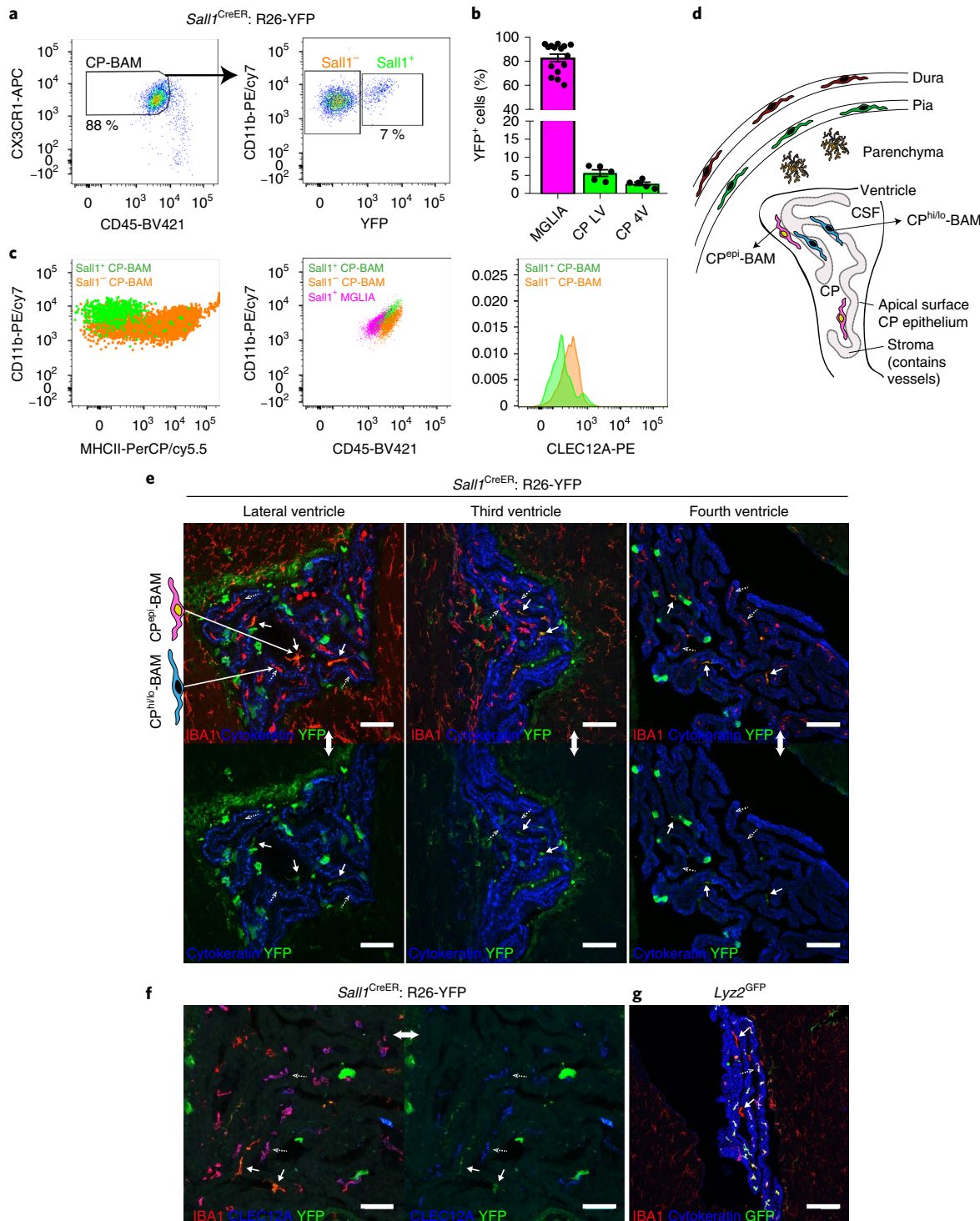


**Fig. 5 |** *Sall1*<sup>+</sup> CP<sup>epi</sup> BAMs reside on the apical surface of the choroid plexus epithelium. **a**, Gating strategy used for identifying *Sall1*<sup>+</sup> CP-BAMs. These were identified using *Sall1*<sup>CreER</sup>; R26-YFP reporter mice. Cells were pre-gated as CD45<sup>+</sup>CD11b<sup>hi</sup> live single cells (as shown in Supplementary Fig. 3d). **b**, Percentage of YFP<sup>+</sup> cells within microglia and lateral and fourth ventricle CP-BAMs. Bars represent mean  $\pm$  s.e.m. of  $n=15$  male/female mice (microglia) and 5 male/female mice (CP). LV, lower ventricle; 4V, fourth ventricle. **c**, Comparison of CD11b and MHCII, CD11b and CD45, and CLEC12A expression between YFP<sup>+</sup> and YFP<sup>-</sup> CP-BAMs. Representative plots of  $n=15$  male/female mice (microglia) and 5 male/female mice (CP). **d**, Legend corresponding to **e–g** showing the in situ location of different BAM subsets. **e–f**, Three-color immunohistochemistry performed on coronal cryosections of brain from tamoxin-injected *Sall1*<sup>CreER</sup>; R26-YFP mice. **e**, Sections containing lateral, third and fourth ventricle CP were stained with anti-IBA1 (red), anti-cytokeratin (blue) and anti-GFP/YFP (green). Top panels show all three channels; bottom panels show green and blue channels only. **f**, Sections containing lateral ventricle CP were stained with anti-IBA1 (red), anti-CLEC12A (blue) and anti-GFP/YFP (green). Left panel shows all three channels; right panel shows green and blue channels only. **g**, Coronal cryosections of adult *Lyz2*<sup>GFP</sup> reporter mice were stained with anti-IBA1 (red), anti-cytokeratin (blue) and anti-GFP/YFP (green). **e–g**, Representative images of  $n=3$  mice; full arrows, IBA1<sup>+</sup> YFP<sup>+</sup> (**e,f**) or GFP<sup>+</sup> (**g**) BAMs on the apical surface of the choroid plexus epithelium (pink in **d**); dashed arrows, IBA1<sup>+</sup> YFP<sup>-</sup> (**e,f**) or GFP<sup>-</sup> (**g**) BAMs within the CP stroma (blue in **d**). Scale bars, 50  $\mu$ m (**e,g**) or 25  $\mu$ m (**f**).

(Fig. 2d,e). Together, these data indicate that CP<sup>epi</sup>-BAMs were epiplexus macrophages, probably representing the elusive Kolmer's epiplexus cells<sup>14</sup>.

**CP<sup>epi</sup>-BAMs from homeostatic brain share a core transcriptional signature with disease-associated microglia (DAM) that are observed under conditions of neurodegeneration.** When directly comparing CP<sup>epi</sup>-BAMs to microglia, a downregulation was seen in microglial signature genes while genes involved in lipid metabolism or phagocytosis, including *Cst7*, *Apoe*, *Clec7a* and *Lpl*, were upregulated (Fig. 6a). Protein expression of APOE and CLEC7A was confirmed in *Sall1*<sup>+</sup> CP<sup>epi</sup>-BAMs (Supplementary Fig. 6a–c). Remarkably, the CP<sup>epi</sup>-BAM gene signature resembled that of DAM, which were recently identified in the 5XFAD Alzheimer's disease model<sup>25</sup>. To compare CP<sup>epi</sup>-BAMs and DAM, we performed scRNA-seq on CD45<sup>+</sup> cells from brains of APP/PS1 AD mice. APP/PS1 brains contained an additional microglial subset (Fig. 6b,c) that exhibited a clear DAM gene signature (Fig. 6d). The number of DAM increased as mice aged, and this subset was not observed in non-transgenic littermate controls (Supplementary Fig. 7a–d). These data confirm that DAM from different Alzheimer's disease models exhibit highly similar gene signatures. Interestingly, the DE genes seen in DAM strongly resembled those of CP<sup>epi</sup>-BAMs. Comparison of the top up- and downregulated genes of both subsets showed that many were shared (Fig. 6e,f). Hence, the core DAM signature is observed not only under conditions of disease but is also induced in CP<sup>epi</sup>-BAMs in healthy young mice. A gene ontology network, based on shared DAM and CP<sup>epi</sup>-BAM signature genes, revealed gene ontologies related to lipid metabolism, leukocyte differentiation/migration and stimulus detection (Fig. 6f).

It is suggested that DAM are phagocytic cells<sup>25,26</sup>. To investigate the phagocytic activity of CP<sup>epi</sup>-BAMs, brain or CP cells from *Sall1*<sup>CreER</sup>:R26-YFP mice were incubated in vitro with pHrodo-labeled *Escherichia coli* bioparticles. Following co-culture, we observed significantly higher pHrodo fluorescence in YFP<sup>+</sup> CP<sup>epi</sup>-BAMs as compared to YFP<sup>+</sup> parenchymal microglia (Fig. 6g,h), indicating that CP<sup>epi</sup>-BAMs exhibit a higher phagocytic activity.

**BAM subsets exhibit a mixed ontogeny and a postnatal development that is highly dependent on the border region.** To investigate how BAM heterogeneity develops over time, we performed flow cytometry on dissected borders starting from postnatal day 0 (Fig. 7a,b). Most BAMs shared a similar phenotype at birth, being MMR<sup>hi</sup> and MHCII<sup>-</sup>. While the SD-BAM pool remained relatively stable, the phenotype and composition of dural and CP-BAMs dramatically changed from postnatal day 21 onwards (Fig. 7a). BAMs downregulated MMR and an MMR<sup>lo</sup>MHCII<sup>hi</sup> population appeared,

which became the predominant subset at 20 weeks (Fig. 7a,b). These changes could have been due to a phenotypical switch of resident BAMs and/or a replacement by bone marrow-derived macrophages. To investigate input from the bone marrow, we performed pulse-chase labeling in *Cx3cr1*<sup>CreER</sup>:R26-YFP mice and examined time-dependent loss of YFP labeling (Fig. 7c). Microglia labeling remained stable, indicating that these cells do not receive peripheral input. Similar observations were made for CP<sup>epi</sup>-BAMs and SD-BAMs. In contrast, YFP labeling gradually declined in dural and CP-BAMs. This was most prominent in D<sup>hi</sup>-BAMs, while a slower decline was observed in D<sup>lo</sup>-BAMs and CP<sup>hi</sup>-BAMs. Next, we used *Flt3*<sup>Cre</sup>:R26-YFP mice, in which *Flt3*-dependent hematopoietic precursors are labeled, allowing for a distinction to be made between embryonically and bone marrow-derived macrophages<sup>27</sup>. At birth, classical monocytes, which are exclusively bone marrow-derived, exhibited only partial YFP labeling due to low *Flt3* promotor activity in embryos<sup>27</sup>, but this rapidly increased (Fig. 7d). Microglia and CP<sup>epi</sup>-BAMs displayed negligible YFP labeling at any of the examined time points, which was confirmed by immunohistochemistry (Fig. 7e). Only a minor fraction of SD-BAMs was YFP<sup>+</sup> (1.4–9.7%). CP<sup>lo</sup>-BAMs also did not display a large increase in YFP labeling, in accordance with the *Cx3cr1*<sup>CreER</sup> pulse-chase experiments (Fig. 7c), but this subset gradually disappeared. Other BAM subsets showed a progressive increase in YFP labeling. As soon as D<sup>hi</sup>-BAMs were observed, the majority were found to be YFP<sup>+</sup> and, at 10 weeks, YFP labeling equalled that of monocytes. Replacement in D<sup>lo</sup>-BAMs and CP<sup>hi</sup>-BAMs occurred more slowly. Together, these results indicate that microglia, CP<sup>epi</sup>-BAMs and SD-BAMs were of embryonic origin while other BAMs were gradually replaced by bone marrow-derived precursors, although with different kinetics depending on the subset and border region.

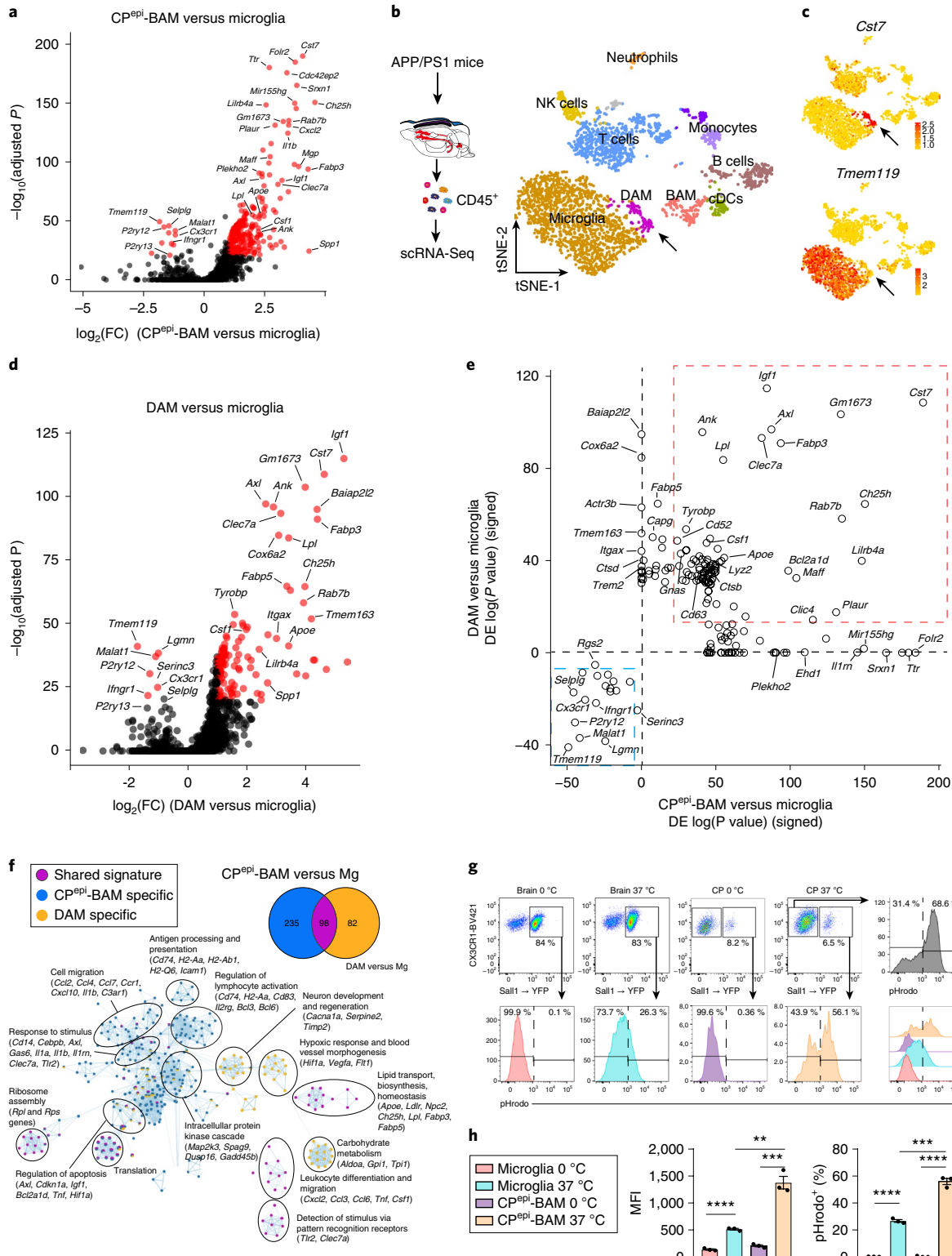
To assess whether the microbiome affects the compositional shift of BAMs, the fraction of MHCII<sup>hi</sup> BAMs was quantified in the dura and CP of germ-free, SPF- and conventionally housed mice at ten weeks of age. This revealed that germ-free animals contained a significantly lower fraction of MHCII<sup>hi</sup> BAMs in the CP and dura (Fig. 7f), suggesting that the microbiome influences BAM development.

Our results suggest that CP<sup>epi</sup>-BAMs and microglia have a shared ontogeny, which would reveal the existence of a microglial subset residing in a non-parenchymal, neuron-free environment. However, our fate-mapping experiments could not exclude that CP<sup>epi</sup>-BAMs originate from embryonically derived *Sall1*<sup>-</sup> CP-BAMs that, throughout life, move from the stroma to the apical CP epithelium and subsequently adopt *Sall1* expression and a microglia-like phenotype. To address this, we first examined whether colony-stimulating factor 1 receptor (CSF1R) inhibition via PLX3397, which depletes

**Fig. 6 | CP<sup>epi</sup>-BAMs share a common transcriptional profile with DAM found in Alzheimer's disease models.** **a**, Volcano plot showing genes that are DE ( $-\log_{10}(\text{adjusted } P) > 20$ ,  $\log_2(\text{FC}) > 1$ ) between CP<sup>epi</sup>-BAM and microglia (shown in red). P value adjustment was performed using Bonferroni correction. **b**, tSNE plot of 3,418 CD45<sup>+</sup> cells from the whole brains of 9-month-old male APP/PS1 mice, showing the presence of a DAM cluster that was identified via unsupervised clustering. **c**, DAM in APP/PS1 mice express *Cst7* and low levels of homeostatic microglial genes such as *Tmem119*. **d**, Volcano plot showing genes that are DE ( $-\log_{10}(\text{adjusted } P) > 20$ ,  $\log_2(\text{FC}) > 1$ ) between DAM and microglia (shown in red). P value adjustment was performed using Bonferroni correction. **e**, Scatter plot comparing the  $\log_{10}(\text{adjusted } P)$  value of the 100 most significantly upregulated genes in CP<sup>epi</sup>-BAMs versus microglia (x axis) and in DAM versus microglia (y axis). The sign of the  $\log_{10}(\text{adjusted } P)$  corresponds to up- or downregulation of genes. Common up- and downregulated genes are found within the red and blue squares, respectively. P value adjustment was performed using Bonferroni correction. **f**, Gene ontology network based on genes that are DE ( $-\log_{10}(\text{adjusted } P) > 10$  and  $\log_2(\text{FC}) > 1$ ) between CP<sup>epi</sup>-BAMs versus microglia or DAM versus microglia (unique and shared genes are displayed in a Venn diagram). Gene ontologies shared by both subsets (purple) or unique to CP<sup>epi</sup>-BAMs (dark blue) or DAMs (orange) are shown. A selection of genes associated with each gene ontology cluster is displayed. **g,h**, Comparison of the phagocytic capacity of CP<sup>epi</sup>-BAMs and microglia in tamoxifen-treated *Sall1*<sup>CreER</sup>:R26-YFP mice using pHrodo-labeled *E. coli* bioparticles. **g**, CP and brain single-cell suspensions were incubated with pHrodo-labeled *E. coli* bioparticles at either 0° or 37°C. Histograms show pHrodo fluorescence in YFP<sup>+</sup> microglia and YFP<sup>+</sup> CP<sup>epi</sup>-BAMs; representative of  $n=3$  biologically independent samples. The experiment was performed twice independently with similar results. **h**, pHrodo median fluorescence intensity (left) and percentage of pHrodo<sup>+</sup> cells (right) in microglia and CP<sup>epi</sup>-BAMs. Bars represent mean  $\pm$  s.e.m. of  $n=3$  biologically independent samples with two male/female adult mice pooled per sample. Significance was evaluated using an unpaired two-tailed t-test. \*\* $P < 0.01$ , \*\*\* $P < 0.001$ , \*\*\*\* $P < 0.0001$ . Statistics can be found in Supplementary Table 2.

parenchymal microglia<sup>28</sup>, also depletes BAMs. Following 21 days of PLX3397 treatment (Fig. 7g), all BAM subsets were almost fully depleted (Fig. 7h,i and Supplementary Fig. 8a). To assess whether this empty niche would repopulate via local self-renewal of surviving macrophages or be reliant on peripheral input, we combined depletion and repopulation with fate-mapping in *Cx3cr1*<sup>CreER</sup>;R26-YFP or *Sall1*<sup>CreER</sup>;R26-YFP mice (Fig. 7g). Four weeks after administration of tamoxifen, when YFP labeling is lost in peripheral

progenitors<sup>24</sup>, *Cx3cr1*<sup>CreER</sup> mice were fed PLX3397-chow for 21 days followed by 10 days of repopulation. All BAMs and microglia almost fully repopulated within this time frame, except for SD-BAMs, which remained strongly depleted (Supplementary Fig. 8b,c). No change was seen in the percentage of YFP labeling in microglia and CP<sup>epi</sup>-BAMs following depletion and repopulation, indicating that these cells fully repopulate via local self-renewal (Fig. 7j). Other BAM subsets showed a significant drop in YFP labeling,



suggesting that repopulation occurred via both the proliferation of local pre-existing YFP<sup>+</sup> macrophages and an influx of peripheral YFP<sup>-</sup> progenitors. However, BAM subsets in the dura and CP exhibited distinct self-renewal capacities, as was evident when comparing the composition of YFP<sup>+</sup> cells in control versus repopulated mice (Supplementary Fig. 8d). When performing depletion and repopulation in *Sall1*<sup>CreER</sup> mice, repopulated microglia remained YFP labeled as expected (Fig. 7k and Supplementary Fig. 8e,f). Importantly, this was also observed for CP<sup>epi</sup>-BAMs. Other BAM subsets did not show any substantial YFP labeling. Together these data show that CP<sup>epi</sup>-BAMs are fully repopulated by a pre-existing *Sall1*<sup>+</sup> cell and originate from neither *Sall1*<sup>-</sup> stromal CP-BAMs nor bone marrow progenitors.

**IRF8 is a master regulator of microglial identity but also shapes the transcriptional maturation of CP-BAMs.** To identify the master regulators that drive the transcriptional program of microglia and BAMs, we used the SCENIC pipeline<sup>29</sup>. SCENIC measures the activity of entire gene regulatory networks or regulons, which are then displayed in activity matrices (Supplementary Fig. 9a-c). tSNE plots were generated based on regulon activity, and cells were colored by their matching Seurat clusters (Fig. 8a). This showed a clear separation between microglia and BAMs and more subtle distinctions between BAMs from different border regions. SCENIC identified known microglial regulators, including *Sall1*, *MafB* and *Irf8*<sup>30-33</sup>. Furthermore, it predicted master regulators that were absent/low in microglia but active in all BAMs or in specific BAM subsets, including *Spic*, *Irf7*, *Maf*, *Etv1* and *Runx3* (Fig. 8b and Supplementary Figs. 9 and 10).

The *Irf8* regulon was predicted to be highly active in microglia but lower in CP<sup>epi</sup>-BAMs (Supplementary Fig. 9c), suggesting that is a regulator of microglial activation. Furthermore, stromal CP-BAMs also exhibited *Irf8* regulon activity (Supplementary Fig. 9c). To investigate the importance of *Irf8*, we specifically deleted it in macrophages using the *Fcgr1*-Cre strain<sup>34</sup>. scRNA-seq was performed on brains or CP from *Fcgr1*<sup>Cre/+</sup>:*Irf8*<sup>loxP/loxP</sup> (Cre<sup>+</sup>) mice or *Fcgr1*<sup>Cre/+</sup>:*Irf8*<sup>loxP/loxP</sup> (Cre<sup>-</sup>) littermate controls (Fig. 8c). Interestingly, microglia, CP<sup>lo</sup>-, CP<sup>hi</sup>- and CP<sup>epi</sup>-BAMs all segregated depending

on the *Fcgr1* genotype (Fig. 8d-f). When comparing Cre<sup>+</sup> to Cre<sup>-</sup> microglia, a strong reduction in microglial signature genes was observed (Fig. 8g,h). Strikingly, *Sall1* expression seemed to be completely abolished (Fig. 8h). Conversely, Cre<sup>+</sup> microglia now exhibited high expression of both BAM signature genes and genes associated with CP<sup>epi</sup>-BAMs or DAM. While Cre recombination of the *Irf8*<sup>loxP/loxP</sup> allele resulted in a truncated messenger RNA that could not be distinguished from the full-length transcript using the 10x genomics 3' assay, SCENIC analysis showed a strong suppression of *Irf8* regulon activity in Cre<sup>+</sup> microglia (Fig. 8i), confirming an IRF8-knockout phenotype. Conversely, IRF8 deletion resulted in increased activity for the BAM-associated regulons *Irf7* and *Runx3* in microglia. Cre<sup>+</sup> microglia also exhibited clear heterogeneity (Supplementary Fig. 11a-d), which may have resulted from temporal dynamics following *Irf8* excision or may have been driven by environmental signals. *Irf8* deletion affected CP<sup>epi</sup>-BAMs in a way similar to that seen for parenchymal microglia, including a further downregulation of microglial signature genes and an induction of BAM signature genes (Fig. 8j,k).

Remarkably, *Irf8* deletion also strongly altered the composition and transcriptional profile of stromal CP-BAMs, although the number of DE genes was lower than for microglia (Supplementary Fig. 11e). While in adult WT mice the majority of stromal CP-BAMs were CP<sup>hi</sup>-BAMs, the opposite was observed in Cre<sup>+</sup> animals (Fig. 8l). Cre<sup>+</sup> CP<sup>lo</sup>-BAMs failed to upregulate genes involved in MHCII expression, and the downregulated genes included the signature gene *Lilra5* (Fig. 8l,m). Conversely, an increase was seen for genes that are normally enriched in MHCII<sup>lo</sup> meningeal BAMs, including *Clec4n* and *Lyve1*. Furthermore, Cre<sup>+</sup> CP<sup>hi</sup>-BAMs exhibited a high expression of *Ccr2* (Fig. 8l), suggesting that all CP<sup>hi</sup>-BAMs in IRF8-knockout animals are monocyte-derived. Together this indicates that, in the absence of IRF8, stromal CP-BAMs fail to transition into the CP<sup>hi</sup> state and maintain a phenotype more akin to that of SD-BAMs or postnatal CP-BAMs.

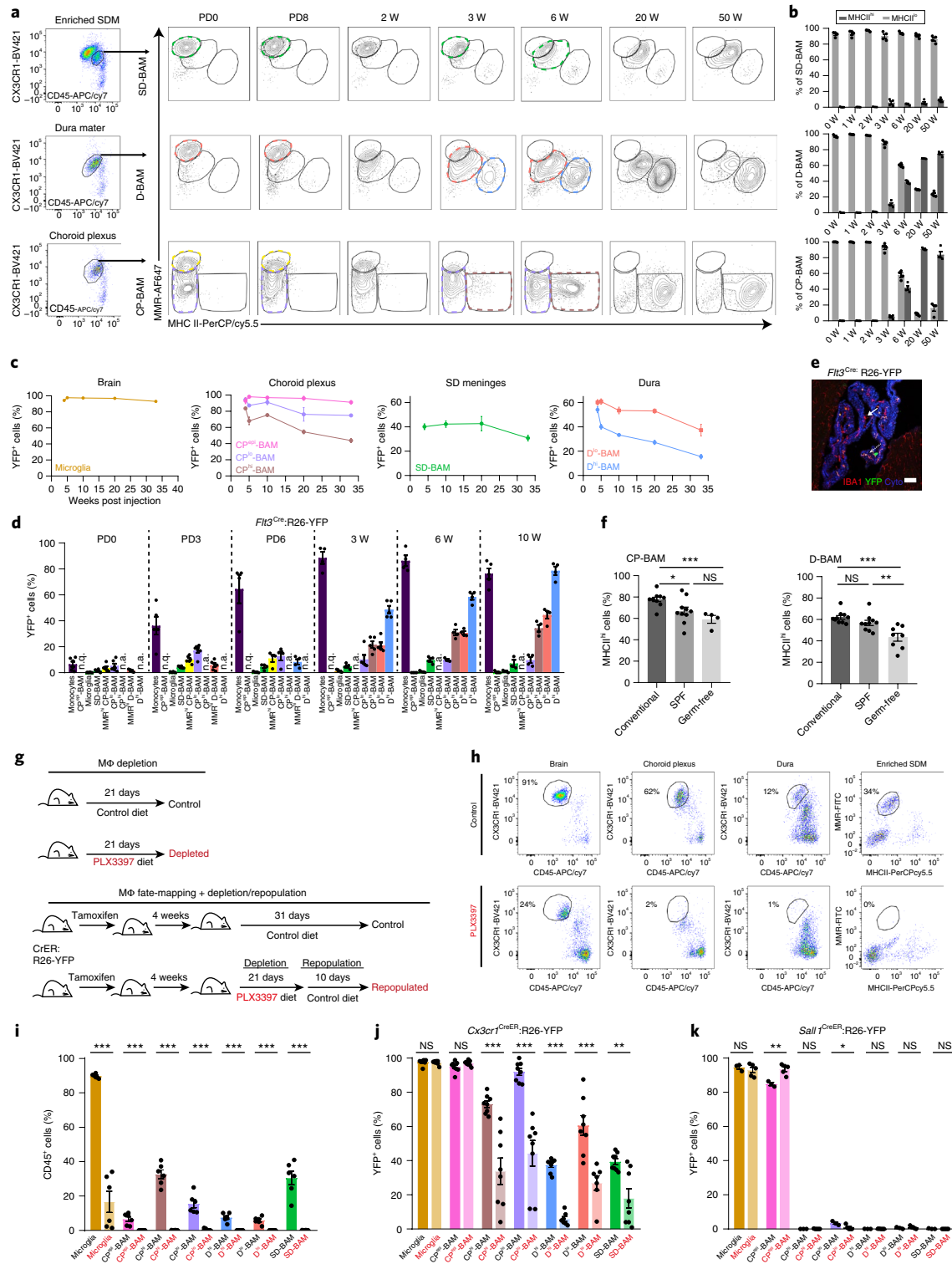
## Discussion

Macrophages are an integral part of all organs and play an instrumental role in regulating tissue homeostasis<sup>11,35</sup>. While seminal

**Fig. 7 | BAM subsets exhibit a mixed ontogeny and display varying self-renewal capacity.** **a**, Kinetic analysis of MMR versus MHCII expression in CX3CR1<sup>hi</sup>CD45<sup>int</sup> BAMs from the enriched SDM, dura and CP from postnatal day (PD) 0 to 50 weeks (W) of age. Cells were pre-gated as CD45<sup>+</sup>CD11b<sup>hi</sup> live single cells (as shown in Supplementary Fig. 3d); representative of  $n=4$  mice per time point. **b**, Percentage of MHCII<sup>hi</sup> cells within the BAM populations between PDO and 50 W. Bars represent the mean  $\pm$  s.e.m. of  $n=4$  animals per time point. **c**, Analysis of YFP dilution over time in adult Cx3cr1<sup>CreER</sup>:R26-YFP mice that received tamoxifen injections at 3–4 weeks of age. Populations were examined between 4 and 33 weeks post-tamoxifen injection via flow cytometry. Each time point represents the mean  $\pm$  s.e.m. of  $n=4$  animals, except  $n=3$  mice at 20 weeks. The decrease in YFP labeling was evaluated with one-way ANOVA. Statistics are included in Supplementary Table 2. **d**, Evaluation of the contribution of bone marrow to BAMs and microglia from PDO to 10 weeks using *Flt3*<sup>Cre</sup>:R26-YFP mice. The Percentage of YFP<sup>+</sup> cells was evaluated with flow cytometry in blood monocytes (CD45<sup>+</sup>CD11b<sup>+</sup>Ly6c<sup>hi</sup>Ly6G<sup>-</sup>, purple) and the indicated brain macrophage populations. The colors correspond to those of the populations in **a**. Bars represent mean  $\pm$  s.e.m. of  $n=6$  (PDO),  $n=6$  (PD3),  $n=4$  (PD6),  $n=5$  (3 weeks),  $n=4$  (6 weeks),  $n=4$  (10 weeks) mice. The increase in YFP labeling was assessed with one-way ANOVA between 3 and 10 weeks. Statistics are included in Supplementary Table 2. **e**, Immunohistochemistry on coronal cryosections, from a 6-week-old *Flt3*<sup>Cre</sup>:R26-YFP mouse, containing lateral ventricle CP. Sections were stained with anti-IBA1 (red), anti-cytokeratin (blue) and anti-GFP/YFP (green). Dashed arrow, YFP<sup>+</sup> stromal CP-BAM; full arrow, YFP<sup>-</sup> CP<sup>epi</sup>-BAM; scale bar, 50  $\mu$ m. Representative image of  $n=4$  mice. **f**, Percentage of MHCII<sup>hi</sup> CP-BAMs and D-BAMs in 10-week-old germ-free, specific-pathogen-free (SPF) and conventional animal facility (conv) C57BL/6 mice. Bars represent mean  $\pm$  s.e.m. of  $n=4$  male/female mice (germ-free CP),  $n=8$  male/female mice (germ-free dura),  $n=10$  male mice (conventional and SPF). The significance was evaluated using an unpaired two-tailed *t*-test. Statistics are included in Supplementary Table 2. **g**, Schematic depiction of (top) PLX3397-based macrophage depletion or (bottom) fate-mapping combined with depletion and repopulation in Cx3cr1<sup>CreER</sup> mice. **h**, Representative flow cytometry plots of whole brain and dissected borders from control and PLX3397-treated C57BL/6 mice (12-week-old males). Cells were pre-gated as CD45<sup>+</sup> live single cells; representative of  $n=6$  mice per condition. **i**, Percentage of BAMs and microglia within the CD45<sup>+</sup> fraction of control (black) and PLX3397-treated (red) mice. Bars represent mean  $\pm$  s.e.m. of  $n=6$  mice. Significance was evaluated using an unpaired two-tailed *t*-test. Statistics are included in Supplementary Table 2. **j**, Percentage of YFP<sup>+</sup> cells in BAMs and microglia from control (black) or repopulated (red) Cx3cr1<sup>CreER</sup>:R26-YFP mice (12- to 14-week-old male/female) that had received tamoxifen injections 4 weeks before depletion and repopulation. Bars represent mean  $\pm$  s.e.m. of  $n=8$  mice ( $n=7$  in dura). Significance was evaluated using an unpaired two-tailed *t*-test. Statistics are included in Supplementary Table 2. **k**, Percentage of YFP<sup>+</sup> cells in BAMs and microglia from control (black) or repopulated (red) *Sall1*<sup>CreER</sup>:R26-YFP mice (11- to 14-week-old male/female) that had received tamoxifen injections before depletion and repopulation. Bars represent mean  $\pm$  s.e.m. of  $n=5$  (repopulated) or  $n=3$  mice (control). Significance was evaluated using an unpaired two-tailed *t*-test. Statistics are included in Supplementary Table 2. NS,  $P > 0.05$ ; \* $P < 0.05$ , \*\* $P < 0.01$ , \*\*\* $P < 0.001$ .

studies have increased our understanding of microglia<sup>12,21,22,36</sup>, macrophages at the brain's border regions have remained elusive. Although originally thought to be short-lived, bone marrow-derived cells, recent work has shown that subdural and perivascular BAMs have an embryonic origin while CP-BAMs have a mixed ontogeny<sup>13</sup>. The ontogeny of dural macrophages was not examined in this study<sup>13</sup>. Furthermore, BAMs were studied as a homogeneous population and it was unclear whether different subsets co-exist that exhibit a distinct ontogeny and/or self-renewal capacity.

Recently, BAM heterogeneity was investigated via mass cytometry at the whole-brain level and four BAM populations were identified based on the differential expression of MHCII, CCR2, CD38 and MMR<sup>8</sup>. Mass cytometry offers valuable high-dimensional protein data and, when combined with intravenous injection of anti-CD45 antibodies, can discriminate between tissue-infiltrating and blood-circulating cells<sup>10</sup>. However, one limitation is the use of a restricted and predefined set of markers. Here, we used single-cell transcriptomics to obtain a genome-wide analysis and an unbiased



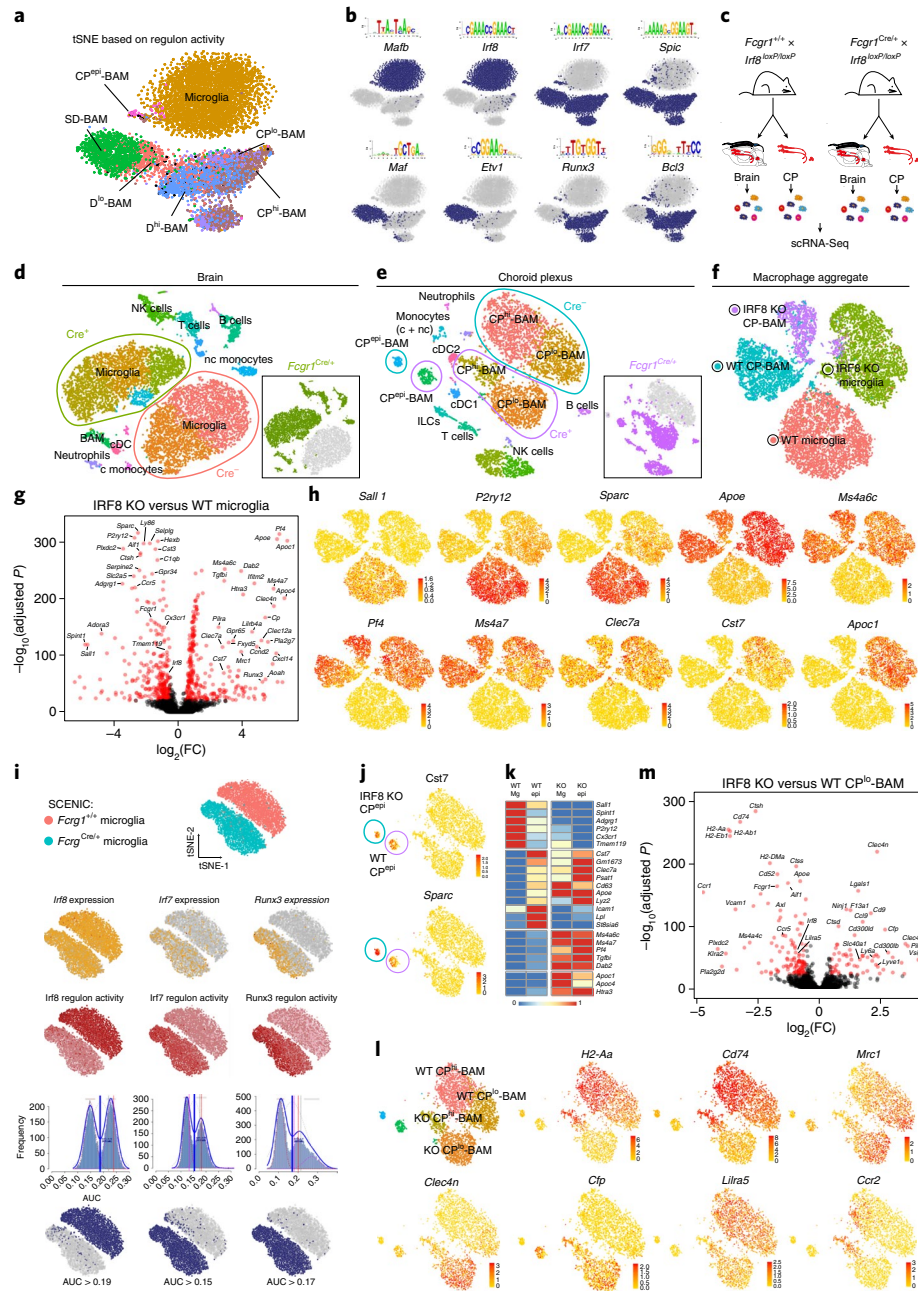


**Fig. 8 | Conditional deletion of Irf8 reveals its pivotal role in regulating the transcriptional program of microglia and CP-BAMs.** **a**, tSNE plot based on the binary regulon activity matrix produced by SCENIC (see Supplementary Fig. 9). Cells are colored based on their designation to clusters in the expression-based tSNE. **b**, tSNE plots showing the activity of the indicated regulons, together with the enriched motif for that transcription factor. Cells in which the indicated regulon is active (that is, regulon activity exceeds a regulon-specific area under the curve (AUC) threshold) are shown in blue. **c**, To target and assess the role of IRF8, brains and CP tissue from *Fcgr1<sup>+/+</sup>;Irf8<sup>loxP/loxP</sup>* and *Fcgr1<sup>Cre/+</sup>;Irf8<sup>loxP/loxP</sup>* mice were used for scRNA-seq. **d**, tSNE plot of 12,078 CD45<sup>+</sup> cells pooled from the brains of *Fcgr1<sup>Cre/+</sup>;Irf8<sup>loxP/loxP</sup>* (*Cre<sup>+</sup>*) and *Fcgr1<sup>+/+</sup>;Irf8<sup>loxP/loxP</sup>* (*Cre<sup>-</sup>*) mice. Cells derived from *Fcgr1<sup>Cre/+</sup>;Irf8<sup>loxP/loxP</sup>* mice are colored green on the inset. Microglia from *Cre<sup>+</sup>* (knockout, KO) or *Cre<sup>-</sup>* (wild-type, WT) mice are circled in green or red, respectively. **e**, tSNE plot of 5,813 CD45<sup>+</sup> cells pooled from the CP of *Fcgr1<sup>Cre/+</sup>;Irf8<sup>loxP/loxP</sup>* and *Fcgr1<sup>+/+</sup>;Irf8<sup>loxP/loxP</sup>* mice. Cells derived from *Fcgr1<sup>Cre/+</sup>;Irf8<sup>loxP/loxP</sup>* are colored purple on the inset. CP-BAMs from *Cre<sup>+</sup>* (KO) and *Cre<sup>-</sup>* (WT) mice are circled in purple and blue, respectively. **f**, tSNE of a macrophage aggregate, consisting of 13,931 macrophages pooled from the whole brain and CP of IRF8 KO/WT mice. Colors correspond to circles in **d,e**. **g**, Volcano plot showing genes that are DE between IRF8-KO and IRF8-WT microglia. Pvalue adjustment was performed using Bonferroni correction. **h**, tSNE maps of the macrophage aggregate showing the expression of several microglia-, BAM- and DAM-signature genes, in addition to genes found exclusively in IRF8-KO CP<sup>epi</sup>-BAMs and microglia. **i**, SCENIC was performed on microglia of *Cre<sup>+</sup>* and *Cre<sup>-</sup>* mice. Top: tSNE plot based on the binary regulon activity matrix. Colors correspond to the origin of the cells. Bottom: plots show the expression of selected transcription factors (yellow plots) and the activity of their corresponding regulons, based on either AUC values (red plots) or a binary plot using regulon-specific AUC cutoffs (blue plots, with cells colored blue when the regulon activity exceeded a regulon-specific AUC threshold, designated by vertical blue lines in the histograms). **j**, tSNE maps of WT and KO CP-BAMs, showing CP<sup>epi</sup>-BAM expression of *Cst7* and *Sparc* in WT (red) and IRF8 KO (blue). **k**, Heatmap of normalized gene expression in IRF8 WT or KO microglia and CP<sup>epi</sup>-BAMs. **l**, tSNE maps of WT and KO CP-BAMs, showing relevant genes that are changed in IRF8 KO and WT CP-BAMs. **m**, Volcano plot showing the genes that are DE between IRF8 KO and WT CP<sup>lo</sup>-BAMs. Pvalue adjustment was performed using Bonferroni correction.

characterization of the cell types found at the brain's border regions. We did not restrict our analysis to whole-brain samples, but included micro-dissected tissue both to reveal regional diversity and to identify potentially minor populations. Our scRNA-seq analysis showed that non-parenchymal macrophages were more heterogeneous than previously observed, and we provide an extensive list of signature genes for their identification. Macrophages in the SDM, dura mater and CP all exhibited tissue-specific signatures, suggesting functional specialization tailored to the needs of the micro-environment. Our results show that at least six BAM subsets were discernible, and we reveal how this heterogeneity developed starting from birth. To build on the work described in ref. <sup>13</sup>, we examined the ontogeny of all individual BAM subsets using various approaches, including fate-mapping combined with CSF1R-mediated depletion and repopulation. This revealed the mixed ontogeny of dural macrophages and showed that BAM subsets have differing self-renewal capacities. Strikingly, both our scRNA-seq and ontogeny results indicated the existence of microglia-like cells residing at the apical surface of the CP epithelium, probably representing the elusive Kolmer's epiplexus cells. Very recently BAM heterogeneity was described via scRNA-seq, which revealed the dynamics and transcriptional changes of the brain's myeloid compartment during neuroinflammation<sup>37</sup>. However, since only a limited number of homeostatic BAMs were profiled and the dura was not included, region-specific transcriptional diversity was less evident and the existence of a population reminiscent of CP<sup>epi</sup>-BAMs was not described.

Macrophage-like cells lining the apical surface of the CP epithelium were previously discovered via electron microscopy and were called Kolmer's epiplexus cells, but their origins and phenotype were unknown<sup>14</sup>. We now show that these epiplexus macrophages, or CP<sup>epi</sup>-BAMs, have a transcriptional signature reminiscent of microglia, expressing highly specific signature genes including *Sall1*, which is absent even in bone marrow-derived microglia<sup>32,38</sup>. We show that, similar to parenchymal microglia<sup>13</sup>, CP<sup>epi</sup>-BAMs are strictly embryonically derived. Therefore, we suggest that CP<sup>epi</sup>-BAMs are a subset of microglia that inhabit the CP epithelial niche. The transcriptional profile of CP<sup>epi</sup>-BAMs exhibited striking similarities to that of DAM<sup>25,26</sup>. The DAM phenotype is suggested to be a common microglial response to brain pathology<sup>39</sup>. Our results now extend this view and show that the core DAM signature is also observed in 'homeostatic' epiplexus microglia in healthy adults. We propose that the core DAM phenotype marks a second 'accessory' function of microglia, which may relate to regulation of tissue homeostasis, metabolism and responses to pathology. The DAM signature has been shown to rely on TREM2/APOE-dependent signaling<sup>25,26,40</sup>. Genes that in DAM were shown to be TREM2-dependent were also upregulated in epiplexus macrophages, suggesting the involvement of the TREM2/APOE pathway in CP<sup>epi</sup>-BAMs as well. Known TREM2 ligands are phospholipids and lipoproteins<sup>41–43</sup>. We speculate that the phenotype of CP<sup>epi</sup>-BAMs, which are in direct contact with CSF and its lipoprotein content, may be shaped through TREM2-based lipid-sensing.

During embryonic development, tissue-resident macrophages may derive from yolk sac macrophages, fetal liver monocytes or hematopoietic stem cells<sup>35</sup>. Following birth, some organs show a progressive replacement of embryonic macrophages by bone marrow-derived cells while other macrophage populations remain of embryonic origin<sup>35</sup>. Our results now show that all dural and stromal CP BAM subsets were gradually replaced by bone marrow-derived progenitors, but that this happened with distinct kinetics. In contrast, CP<sup>epi</sup>-BAMs and SD-BAMs were not replaced by monocytes. This indicates that, at steady state, the macrophage pool in the brain's more permeable regions (dura mater and CP stroma) showed bone marrow replacement while this did not occur in the brain's closed tissues (parenchyma, SDM and the apical surface of the CP epithelium). This suggests that tissue accessibility is a major determinant for brain macrophage ontogeny. However, after

BAMs were depleted via CSF1R blockade, repopulation in the CP and dura still occurred to a large extent via the expansion of local macrophages. This reveals the high self-renewal capacity of certain BAM subsets and suggests that, even in brain regions that lack barriers, a fraction of embryonic macrophages persists throughout life. Surprisingly, SD-BAMs exhibited marked difficulty in repopulating the empty niche following depletion, suggesting a limited or delayed self-renewal capacity. The only macrophage subsets that repopulated independently of bone marrow progenitors were microglia and CP<sup>epi</sup>-BAMs, which were fully derived from local *Sall1*<sup>+</sup> macrophages. It is currently unknown whether microglial progenitors seed the CP during embryonic development and, in adults, self-renew in situ or whether throughout life there is a migration of microglia from the subependymal parenchyma into the CP.

To reveal the gene regulatory networks and master transcription factors that drive the divergence between microglia and BAMs, we performed SCENIC analysis and selected *Irf8* for conditional gene knockout studies. IRF8 deficiency is known to result in the abnormal development and functional alterations of a wide range of myeloid cells, including microglia<sup>44–48</sup>. By examining macrophage-specific IRF8-knockout brains, we show that much of the transcriptional divergence between microglia and BAMs is regulated by *Irf8*, which suppresses the general BAM transcriptional signature in microglia. Interestingly, it was recently shown that at embryonic day 14.5 a fraction of microglia express BAM signature genes<sup>49</sup>, suggesting that IRF8-driven maturation of microglia may start around this developmental period. In addition, IRF8 deficiency resulted in the expression of CP<sup>epi</sup>-BAM signature genes in microglia, indicating that this regulates the transition between these two microglial states. Interestingly, IRF8-deficient stromal CP-BAMs maintained a phenotype closer to MHCII<sup>lo</sup> meningeal BAMs or postnatal CP-BAMs. Together, this indicates that IRF8 is critically involved in driving the maturation and diversity of brain macrophages.

## Online content

Any methods, additional references, Nature Research reporting summaries, source data, statements of code and data availability and associated accession codes are available at <https://doi.org/10.1038/s41593-019-0393-4>.

Received: 9 July 2018; Accepted: 21 March 2019;

Published online: 6 May 2019

## References

- Shechter, R., London, A. & Schwartz, M. Orchestrated leukocyte recruitment to immune-privileged sites: absolute barriers versus educational gates. *Nat. Rev. Immunol.* **13**, 206–218 (2013).
- Engelhardt, B., Vajkoczy, P. & Weller, R. O. The movers and shapers in immune privilege of the CNS. *Nat. Immunol.* **18**, 123–131 (2017).
- Louveau, A. et al. Structural and functional features of central nervous system lymphatic vessels. *Nature* **523**, 337–341 (2015).
- Aspelund, A. et al. A dural lymphatic vascular system that drains brain interstitial fluid and macromolecules. *J. Exp. Med.* **212**, 991–999 (2015).
- Nabeshima, S., Reese, T. S., Landis, D. M. D. & Brightman, M. W. Junctions in the meninges and marginal glia. *J. Comp. Neurol.* **164**, 127–169 (1975).
- Balin, B. J., Broadwell, R. D., Salcman, M. & El-Kalliny, M. Avenues for entry of peripherally administered protein to the central nervous system in mouse, rat, and squirrel monkey. *J. Comp. Neurol.* **251**, 260–280 (1986).
- Wolburg, H. & Paulus, W. Choroid plexus: biology and pathology. *Acta Neuropathol.* **119**, 75–88 (2010).
- Mrdjen, D. et al. High-dimensional single-cell mapping of central nervous system immune cells reveals distinct myeloid subsets in health, aging, and disease. *Immunity* **48**, 380–395 (2018).
- Ajami, B. et al. Single-cell mass cytometry reveals distinct populations of brain myeloid cells in mouse neuroinflammation and neurodegeneration models. *Nat. Neurosci.* **21**, 541–551 (2018).
- Korin, B. et al. High-dimensional, single-cell characterization of the brain's immune compartment. *Nat. Neurosci.* **20**, 1300–1309 (2017).
- Okabe, Y. & Medzhitov, R. Tissue biology perspective on macrophages. *Nat. Immunol.* **17**, 9–17 (2016).

12. Prinz, M. & Priller, J. Microglia and brain macrophages in the molecular age: from origin to neuropsychiatric disease. *Nat. Rev. Neurosci.* **15**, 300–312 (2014).
13. Goldmann, T. et al. Origin, fate and dynamics of macrophages at central nervous system interfaces. *Nat. Immunol.* **17**, 797–805 (2016).
14. Ling, E.-A., Kaur, C. & Jia, L. Origin, nature, and some functional considerations of intraventricular macrophages, with special reference to the epiplexus cells. *Microsc. Res. Tech.* **41**, 43–56 (1998).
15. Guilliams, M. et al. Unsupervised high-dimensional analysis aligns dendritic cells across tissues and species. *Immunity* **45**, 669–684 (2016).
16. Miller, J. C. et al. Deciphering the transcriptional network of the dendritic cell lineage. *Nat. Immunol.* **13**, 888–899 (2012).
17. Mildner, A. et al. Genomic characterization of murine monocytes reveals C/EBP $\beta$  transcription factor dependence of Ly6C $^{-}$  cells. *Immunity* **46**, 849–862.e7 (2017).
18. van den Brink, S. C. et al. Single-cell sequencing reveals dissociation-induced gene expression in tissue subpopulations. *Nat. Methods* **14**, 935–936 (2017).
19. Haimon, Z. et al. Re-evaluating microglia expression profiles using RiboTag and cell isolation strategies. *Nat. Immunol.* **19**, 636–644 (2018).
20. Wu, Y. E., Pan, L., Zuo, Y., Li, X. & Hong, W. Detecting activated cell populations using single-cell RNA-Seq. *Neuron* **96**, 313–329.e6 (2017).
21. Hickman, S. E. et al. The microglial sensome revealed by direct RNA sequencing. *Nat. Neurosci.* **16**, 1896–1905 (2013).
22. Butovsky, O. et al. Identification of a unique TGF- $\beta$ -dependent molecular and functional signature in microglia. *Nat. Neurosci.* **17**, 131–143 (2013).
23. Cannoodt, R., et al. SCORPIUS improves trajectory inference and identifies novel modules in dendritic cell development. Preprint at *bioRxiv* <https://www.biorxiv.org/content/10.1101/079509v2> (2016).
24. Goldmann, T. et al. A new type of microglia gene targeting shows TAK1 to be pivotal in CNS autoimmune inflammation. *Nat. Neurosci.* **16**, 1618–1626 (2013).
25. Keren-Shaul, H. et al. A unique microglia type associated with restricting development of Alzheimer's disease. *Cell* **169**, 1276–1290.e17 (2017).
26. Krasemann, S. et al. The TREM2-APOE pathway drives the transcriptional phenotype of dysfunctional microglia in neurodegenerative diseases. *Immunity* **47**, 566–581.e9 (2017).
27. Gomez Perdiguero, E. et al. Tissue-resident macrophages originate from yolk-sac-derived erythro-myeloid progenitors. *Nature* **518**, 547–551 (2014).
28. Elmore, M. R. P. et al. Colony-stimulating factor 1 receptor signaling is necessary for microglia viability, unmasking a microglia progenitor cell in the adult brain. *Neuron* **82**, 380–397 (2014).
29. Aibar, S. et al. SCENIC: single-cell regulatory network inference and clustering. *Nat. Methods* **14**, 1083–1086 (2017).
30. Lavin, Y. et al. Tissue-resident macrophage enhancer landscapes are shaped by the local microenvironment. *Cell* **159**, 1312–1326 (2014).
31. Matcovich-Natan, O. et al. Microglia development follows a stepwise program to regulate brain homeostasis. *Science* **353**, aad8670 (2016).
32. Buttigereit, A. et al. Sall1 is a transcriptional regulator defining microglia identity and function. *Nat. Immunol.* **17**, 1397–1406 (2016).
33. Kierdorf, K. et al. Microglia emerge from erythromyeloid precursors via Pu.1- and Irf8-dependent pathways. *Nat. Neurosci.* **16**, 273–280 (2013).
34. Scott, C. L. et al. The transcription factor ZEB2 is required to maintain the tissue-specific identities of macrophages. *Immunity* **49**, 312–325.e5 (2018).
35. Ginhoux, F. & Guilliams, M. Tissue-resident macrophage ontogeny and homeostasis. *Immunity* **44**, 439–449 (2016).
36. Gosselin, D. et al. An environment-dependent transcriptional network specifies human microglia identity. *Science* **356**, 1248–1259 (2017).
37. Jordão, M. J. C. et al. Single-cell profiling identifies myeloid cell subsets with distinct fates during neuroinflammation. *Science* **363**, eaat7554 (2019).
38. Cronk, J. C. et al. Peripherally derived macrophages can engraft the brain independent of irradiation and maintain an identity distinct from microglia. *J. Exp. Med.* **215**, 1627–1647 (2018).
39. Deczkowska, A. et al. Disease-associated microglia: a universal immune sensor of neurodegeneration. *Cell* **173**, 1073–1081 (2018).
40. Butovsky, O. et al. Targeting miR-155 restores abnormal microglia and attenuates disease in SOD1 mice. *Ann. Neurol.* **77**, 75–99 (2015).
41. Song, W. et al. Alzheimer's disease-associated TREM2 variants exhibit either decreased or increased ligand-dependent activation. *Alzheimer's Dement.* **13**, 381–387 (2017).
42. Wang, Y. et al. TREM2 lipid sensing sustains the microglial response in an Alzheimer's disease model. *Cell* **160**, 1061–1071 (2015).
43. Yeh, F. L., Wang, Y., Tom, I., Gonzalez, L. C. & Sheng, M. TREM2 binds to apolipoproteins, including APOE and CLU/APOJ, and thereby facilitates uptake of amyloid-beta by microglia. *Neuron* **91**, 328–340 (2016).
44. Tamura, T., Kurotaki, D. & Koizumi, S. Regulation of myelopoiesis by the transcription factor IRF8. *Int. J. Hematol.* **101**, 342–351 (2015).
45. Sichien, D. et al. IRF8 transcription factor controls survival and function of terminally differentiated conventional and plasmacytoid dendritic cells, respectively. *Immunity* **45**, 626–640 (2016).
46. Hagemeyer, N. et al. Transcriptome-based profiling of yolk sac-derived macrophages reveals a role for Irf8 in macrophage maturation. *EMBO J.* **35**, 1730–1744 (2016).
47. Masuda, T. et al. IRF8 is a critical transcription factor for transforming microglia into a reactive phenotype. *Cell Rep.* **1**, 334–340 (2012).
48. Masuda, T. et al. IRF8 is a transcriptional determinant for microglial motility. *Purinergic Signal.* **10**, 515–521 (2014).
49. Hammond, T. R. et al. Single-cell RNA sequencing of microglia throughout the mouse lifespan and in the injured brain reveals complex cell-state changes. *Immunity* **50**, 253–271.e6 (2019).

## Acknowledgements

This work was supported by Innoviris (Attract grant No. BB2B 2015-2) and Fonds Wetenschappelijk Onderzoek (grant No. 1506316N) to K.M. and a VLAIO grant (No. ImmCyte HBC.2016.0889) to K.M., J.A.vG., J.A. and D.M. H.V.H. is supported by an FWO predoctoral fellowship (No. 1163218N). Y.S. is an ISAC Marylou Ingram Scholar. We thank Y. Elkrim for technical assistance, M. Kiss for helpful discussions, VIB BioImaging Core for support regarding microscopy and VIB Tech Watch for support and funding with regard to scRNA-seq technologies.

## Author contributions

H.V.H. and K.M. conceived the study and designed experiments. H.V.H., I.S., K.D.V., A.R.P.A., S.D.P., N.V., S.D.S., G.V.I., C.L.S., J.A., R.E.V., L.V. and K.M. performed experiments. L.M. developed analysis algorithms and the online tool. H.V.H., L.M., I.S., Y.S. and K.M. carried out analyses. C.L.S., G.E.B., L.V., D.M. and M.G. provided important reagents. G.B., G.E.B., R.E.V., D.M., M.G., J.A.vG. and Y.S. provided important advice on experimental design, data analysis and interpretation. H.V.H and K.M. wrote the manuscript. I.S., D.M., M.G., J.A.vG. and Y.S. revised the manuscript. K.M. directed the study.

## Competing interests

The authors declare no competing interests.

## Additional information

**Supplementary information** is available for this paper at <https://doi.org/10.1038/s41593-019-0393-4>.

**Reprints and permissions information** is available at [www.nature.com/reprints](http://www.nature.com/reprints).

**Correspondence and requests for materials** should be addressed to K.M.

**Journal peer review information:** *Nature Neuroscience* thanks Jonathan Kipnis and the other anonymous reviewer(s) for their contribution to the peer review of this work.

© The Author(s), under exclusive licence to Springer Nature America, Inc. 2019

## Methods

**Mice.** C57BL/6J mice were either bred in house or bought from Janvier. Males (Janvier) aged 7 and 9 weeks were used for bulk RNA-sequencing and 10x chromium scRNA-seq, respectively. Additional mouse lines used for scRNA-seq experiments were: male 9- or 16-month-old APP/PS1 (ref. <sup>20</sup>) together with 16-month-old non-transgenic controls, female 7–11-week-old *Fcgr1*<sup>Cre/+</sup> (ref. <sup>34</sup>) × *Irf8*<sup>loxP/loxP</sup> (ref. <sup>45</sup>) and *Fcgr1*<sup>+/+</sup> × *Irf8*<sup>loxP/loxP</sup> littermates. For FACSymphony experiments, 9-week-old males from Janvier were used. Ten-week-old male/female germ-free C57BL/6 mice were bred in the Ghent Germfree and Gnotobiotic mouse facility (Ghent University, Belgium). Germ-free mice were bred in hepa-filtered, flexible-film isolators (North Kent Plastics). Germ-free status was routinely monitored by culture-dependent and -independent methods. *Cx3cr1*<sup>CreER</sup> (ref. <sup>24,51</sup>), *Flt3*<sup>Cre</sup> (ref. <sup>52</sup>) *Sall1*<sup>CreER</sup> (ref. <sup>53</sup>) and R26-YFP<sup>54</sup> mice were bred in house. The sex and ages of the animals used are indicated in the Figure legends. Details regarding the strain, sex and age of mice used within this study can be found within the Reporting Summary. Mouse experiments were approved and performed in accordance with the Ethische Commissie Dierproeven at Vrije Universiteit Brussel.

**Whole-brain, CP, dura and enriched SDM single-cell isolation.** Mice were deeply anaesthetized and perfused transcardially with 30 ml of ice-cold phosphate buffered saline (PBS). For whole-brain isolation, mice were decapitated and brains were placed on ice-cold Roswell Park Memorial Institute (RPMI) 1640 medium (Gibco). Brains were cut into small pieces followed by the addition of enzyme mix (30 U ml<sup>-1</sup> DNase I (Roche), 10 U ml<sup>-1</sup> collagenase type I (Worthington) and 400 U ml<sup>-1</sup> collagenase type IV (Worthington) diluted in 1× Hanks' buffered salt solution (Gibco)). Following 20 min at 37°C, tissue was crushed with a syringe plunger and homogenized via trituration using standard serological pipettes. The solution was filtered twice over a 100 µm nylon filter and centrifuged. The pellet was resuspended in 5 ml 70% standard isotonic percoll (SIP, GE Healthcare) diluted in 1× Hanks' buffered salt solution and gently overlaid with 5 ml of 37% SIP, followed by a 5 ml layer of 30% SIP, forming a three-layered density gradient (centrifuged at 800g, 4°C, 30 min without acceleration/braking). The 70/37% interphase containing immune cells was collected, centrifuged and resuspended in fluorescent activated cell sorter (FACS) buffer (2 mM EDTA (Duchefa), 2% heat-inactivated fetal calf serum (Gibco) dissolved in 1× Hanks' buffered salt solution). The dissociation process lasted 4 h.

For isolation of the dura mater, the dorsal part of the skull was carefully removed. The dura was peeled off from the skull cap and placed in ice-cold RPMI. The enriched SDM were isolated by manually cutting a thin slice of the dorsal cortex using a 0.25 mm low-profile disposable blade 918 (Leica BioSystems). The slice comprised the area between bregma coordinates 2 and –4 mm and was <1 mm thick, weighing ±5 mg. For isolation of the CP, the ventricles were exposed after which the CP of the lateral and fourth ventricles was carefully micro-dissected and placed in ice-cold RPMI. The CP, dura and enriched SDM were cut into small pieces and incubated with enzyme mix at 37°C for 30 min (the solution was resuspended every 10 min). Next, solutions were filtered and centrifuged. Cells from the dura and CP were resuspended in FACS buffer. To remove myelin, cells from the enriched SDM were resuspended in 30% SIP and centrifuged (800g, 4°C, 30 min, no acceleration/braking), and the pellet was resuspended in FACS buffer. The dissociation process required 135 min for the dura and CP and 3 h for the SDM.

To assess for and limit the induction of dissociation-induced gene expression, we adjusted the protocol described above with ActD modifications based on ref. <sup>20</sup>. For the ActD isolation protocol, the CP and dura were dissected as mentioned above and placed in ice-cold RPMI containing 30 µM ActD (Sigma, No. A1410). The CP and dura were cut into small pieces and incubated with enzyme mix containing 15 µM ActD at 11°C for 50 min. Every 10 min the solution was cut and resuspended to ensure full dissociation of the tissue. The remaining process was performed as stated previously, with ActD added in three steps. Filtering was performed with RPMI containing 3 µM ActD. The pellet was resuspended in FACS buffer containing 3 µM ActD, and sorted cells were collected in ME medium (RPMI medium supplemented with 20% heat-inactivated fetal calf serum (Gibco), 300 µg ml<sup>-1</sup> L-glutamine (Gibco), 100 units ml<sup>-1</sup> penicillin and 100 µg ml<sup>-1</sup> streptomycin (Gibco), 1 mM non-essential amino acids (Gibco), 1 mM sodium pyruvate (Gibco) and 0.05 mM 2-mercaptoethanol (Sigma)) containing 3 µM ActD. The dissociation process required 135 min. Cells were kept on ice during all steps, except for the enzymatic digestion. Samples that were processed using ActD were compared to those processed using the standard protocol as described above.

**Isolation of peritoneal and alveolar macrophages, Kupffer cells and blood cells.** Mice were killed with CO<sub>2</sub>, after which peritoneal lavage was performed with 10 ml ice-cold PBS. The solution was centrifuged (450g, 5 min, 4°C) and the pellet was resuspended in FACS buffer. Alveolar macrophages and Kupffer cells were isolated as described previously<sup>34</sup>. Blood was withdrawn through either heart puncture or the tail vein using heparin-filled syringes. Red blood cells were lysed using lysis buffer (155 mM NH<sub>4</sub>Cl, 10 mM KHCO<sub>3</sub>, 500 mM EDTA) followed by neutralization with RPMI and resuspension in FACS buffer.

**scRNA-sequencing using 10x Genomics platform.** Single-cell suspensions derived from the dura, CP, SDM and whole brain were obtained using procedures described above. All processing was performed at temperatures <4°C except for enzymatic digestion, which varied depending on the protocol (standard or ActD, see above). For WT C57BL/6 experiments (standard isolation protocol) we pooled the following: whole brains from four individual mice, enriched SDM and dura from 18 individual mice and CP (from the lateral and fourth ventricles) from 21 individual mice (9-week-old males). For scRNA-seq comparison between our standard and ActD protocols, we pooled the following: dura and CP (from the lateral and fourth ventricles) from ten individual mice for each protocol (standard versus ActD isolation protocol) (9-week-old male C57BL/6). For *Irf8*<sup>KO</sup> experiments (standard isolation protocol) we pooled the following: brains (with CP removed) from four *Fcgr1*<sup>Cre/+</sup> × *Irf8*<sup>loxP/loxP</sup> or four *Fcgr1*<sup>+/+</sup> × *Irf8*<sup>loxP/loxP</sup> mice and CP from seven *Fcgr1*<sup>Cre/+</sup> × *Irf8*<sup>loxP/loxP</sup> or eight *Fcgr1*<sup>+/+</sup> × *Irf8*<sup>loxP/loxP</sup> mice (7- to 11-week-old females). For APP/PS1 experiments (standard isolation protocol) we pooled whole brains from the following: two individual 9-month-old APP/PS1 mice, two 16-month-old APP/PS1 mice and two 16-month-old C57BL/6 non-transgenic controls. Following single-cell isolation, cells were stained with anti-CD45-APC/Cy7 for 20 min on ice, washed and CD45<sup>+</sup> immune cells were then sorted from each tissue using a BD FACS ARIA III. Because estimates of macrophage size were around 8–15 µm, an 85 µm nozzle was used for sorting. Between 7 and 15 min was required to sort CD45<sup>+</sup> cells from border regions, and 5 min for whole-brain samples. Typically around 50,000 cells were sorted per sample, in ME medium. DAPI (Sigma) was used to exclude dead cells; cell viability before and after cell sorting exceeded 90%. Sorted cells were centrifuged at 4°C at 400g, then resuspended in PBS + 0.04% bovine serum albumin at room temperature to yield an estimated final concentration of 1,000 cells µl<sup>-1</sup>. Cellular suspensions were loaded on a GemCode Single Cell Instrument (10x Genomics) to generate single-cell gel beads-in-emulsion (GEM). GEMs and scRNA-seq libraries were prepared using the GemCode Single Cell 3' Gel Bead and Library Kit (10x Genomics, No. 120237) and the Chromium i7 Multiplex Kit (10x Genomics, No. 120262) according to the manufacturer's instructions. Briefly, GEM reverse-transcription incubation was performed in a 96-deep-well reaction module at 53°C for 45 min, 85°C for 5 min and ending at 4°C. Next, GEMs were broken and complementary DNA (cDNA) was cleaned up with DynaBeads MyOne Silane Beads (Thermo Fisher Scientific, No. 37002D) and SPRIselect Reagent Kit (Beckman Coulter, No. B23318). Full-length, barcoded cDNA was PCR amplified with a 96-deep-well reaction module at 98°C for 3 min, ten cycles at 98°C for 15 s, 67°C for 20 s and 72°C for 1 min, one cycle at 72°C for 1 min and ending at 4°C. Following cleaning up with the SPRIselect Reagent Kit and enzymatic fragmentation, library construction to generate Illumina-ready sequencing libraries was performed by the addition of R1 (read 1 primer), P5, P7, i7 sample index and R2 (read 2 primer sequence) via end-repair, A-tailing, adapter ligation, post-ligation SPRIselect cleanup/size selection and sample index PCR. The cDNA content of pre-fragmentation and post-sample index PCR samples was analyzed using the 2100 BioAnalyzer (Agilent). Each scRNA-seq experiment was performed once, giving rise to 15 individual scRNA-seq libraries that were created in this study, totaling over 61,000 single cells.

Sequencing libraries were loaded on an Illumina HiSeq4000 flow cell with sequencing settings following the recommendations of 10x Genomics (read 1: 26 cycles; read 2: 98 cycles; index i7: eight cycles; index i5: no cycles; 2.1 pM loading concentration). The Cell Ranger pipeline was designed to perform sample demultiplexing and to generate FASTQ files for read 1, read 2 and the i7 sample index. Read 2, containing the cDNA, was mapped to the reference genome (mouse mm10) using STAR. Subsequent barcode processing, unique molecular identifiers filtering and single-cell 3' gene counting was performed using the Cell Ranger suite and Seurat v.2.3. The average of the mean reads per cell across all libraries was >65,000, with an average sequencing saturation metric of >80%, as calculated by Cell Ranger. Aggregation of sample conditions was done using the Cell Ranger Aggr software from 10x Genomics. Digital gene expression matrices were preprocessed and filtered using the SCran and Scater R packages<sup>55</sup>. Outlier cells were first identified based on three metrics (library size, number of expressed genes and mitochondrial proportion); cells were tagged as outliers when they were four median absolute deviations distant from the median value of each metric across all cells. Secondly, a principal component analysis plot was generated based on the following metrics: 'pct\_counts\_in\_top\_100\_features', 'total\_features\_by\_counts', 'pct\_counts\_feature\_control', 'total\_features\_by\_counts\_feature\_control', 'log10\_total\_counts\_endogenous' and 'log10\_total\_counts\_feature\_control'. Outlier cells in this principal component analysis plot were identified using the R package mvoutlier. Low-abundance genes were removed using the 'calcAverage' function and the proposed workflow. The raw counts were normalized and log<sub>2</sub> transformed by first calculating 'size factors' that represented the extent to which counts should be scaled in each library. Highly variable genes were detected using the proposed workflow of the scran R package and by applying false discovery rate ≤0.05 and var.out\$bio ≥0.01 as cutoffs. Highly variable genes were subsequently used for unsupervised dimensionality reduction techniques and principal component analysis. Unsupervised clustering of the cells was performed using graph-based clustering based on SNN-Clip<sup>56</sup> and PhenoGraph<sup>57</sup> as implemented in the Seurat v.2.3 R package<sup>58</sup> (default parameters). Clustering was visualized in two-dimensional scatter plots (via tSNE) using the Seurat v.2.3 R package.

We observed the induction of IEGs in some of the CD45<sup>+</sup> cells, which was most obvious in CP samples where two clearly separated macrophage clusters were observed that differed only in the expression of IEGs and heat shock proteins. These differentially expressed genes closely resembled those identified in a subset of muscle satellite cells, which were shown to be dissociation-induced genes<sup>18</sup>. To confirm that in our samples the observed IEGs were also dissociation induced, we compared single-cell isolation using either a standard or ActD modified protocol (see above). IEG expression was blocked in ActD samples, which allowed us to identify 224 genes that were upregulated in standard versus ActD samples, in both dura and CP BAMs, comprising the dissociation-induced gene list (Supplementary Table 3). To correct for dissociation-induced gene expression, which may mask biologically relevant results, we used this gene list to detect cells that were ‘dissociation affected’ by plotting the expression of all these genes over all cells. When plotting this as a histogram, a clear cutoff was seen that split the cells in ‘dissociation-affected’ and non-affected cells. In contrast to the workflow proposed in ref. <sup>18</sup>, we did not remove the dissociation-affected cells but added this information to the metadata attribute of the Seurat object, so we subsequently could remove this unwanted source of variation using the ‘Regress out’ function of the Seurat R package. An alternative approach to correct for dissociation-induced effects was to remove these 224 genes from the highly variable gene list used for subsequent unsupervised dimensionality reduction techniques and clustering algorithms (see above), as previously done in ref. <sup>20</sup>.

In all samples, small clusters were identified that exhibited the simultaneous expression of both macrophage and lymphocyte genes. These clusters were assumed to be macrophage–lymphocyte aggregates and were excluded from analysis.

We noticed that *Clec7a* is not present in the mm10 reference dataset provided by 10x Cell Ranger. As our attempt to create a new Cell Ranger mm10 reference dataset with the inclusion of *Clec7a* failed, we used Kallisto<sup>29</sup> with default parameters to map the expression of *Clec7a*. We filtered the SAM output file from Kallisto for the two transcripts of *Clec7a* (ENSMUST00000184581.2 and ENSMUST00000112076.8). The read headers from this filtered SAM file were then mapped to the R1 FASTQ file (Cell Ranger mkfastq output) to get the 26 base pair (bp) read 1 (16 bp chromium barcode and 10 bp unique molecular identifiers). We extracted the 16 bp cell barcode from this 26 bp read and colored these cells on the tSNE plot. To estimate the expression of *Clec7a*, we counted the number of times a cell barcode was present and used this value as raw count input.

**Trajectory inference using SCORPIUS.** SCORPIUS was performed on classical monocytes (Cl. Monocytes), monocyte-derived cells (MdC), D<sup>hi</sup>-BAM and D<sup>lo</sup>-BAM clusters of the dura mater sample. We started from the log<sub>2</sub> normalized counts (via the scran R package), selected the clusters of interest and performed SCORPIUS using the proposed workflow<sup>23</sup>.

**Single-cell regulatory network inference and clustering using SCENIC.** We performed SCENIC<sup>29</sup> by starting from the raw counts and following the proposed workflow using the default parameters. The co-expression network was generated using GENIE3 rather than GRNBoost2. AUC, which identifies and scores gene regulatory networks or regulons in single cells, was calculated using AUCell as previously described<sup>29</sup>. The better the targets of a regulon match the highly expressed genes of a certain cell, the higher the AUC value of that regulon in that particular cell. Besides plotting binary expression matrices<sup>29</sup>, we also transformed these AUC values into values ranging from 0 to 1 for each regulon, plotted this in a heatmap with a blue–red color scale and performed hierarchical clustering on the rows using the pheatmap R package. The regulons were visualized in a network using iRegulon v.1.3 (ref. <sup>60</sup>) in Cytoscape v.3.5.1. (ref. <sup>61</sup>). Motifs were obtained from iRegulon v.1.3 (ref. <sup>60</sup>).

**Flow cytometry and FACSymphony.** After obtaining a single-cell suspension, live-dead staining was performed using Zombie Aqua Fixable Live-dead (BioLegend) following the manufacturer’s protocol. Subsequently cells were blocked with rat anti-mouse CD16/CD32 (clone 2.4G2) for 15 min on ice and stained for 20 min using the antibodies listed in Supplementary Table 4. Intracellular antigen staining was performed with the eBioscience Foxp3/ Transcription Factor Staining Buffer kit (Thermo Fisher Scientific, No. 00-5523-00) following the manufacturer’s instructions. After staining, cells were washed with FACS buffer. The FACSymphony experiments were repeated three independent times and were analyzed using the BD FACSymphony A5. Before acquisition, photomultiplier tube voltages were adjusted to minimize fluorescence spillover. Single-stain controls were prepared with UltraComp eBeads (Thermo Fisher Scientific) following the manufacturer’s instructions, and were used to calculate a compensation matrix. Other flow cytometry experiments were performed using the BD FACS Canto II.

Flow cytometry data was analyzed using FlowJo\_V10 and Cytobank (<https://www.cytobank.org>).

**Bulk RNA-seq.** The various macrophage populations were isolated using the above-mentioned procedures. Sample sizes were chosen according to ref. <sup>32</sup>. Single-cell suspensions were blocked with anti-mouse CD16/CD32 (clone 2.4G2)

and stained. Dead cells were excluded using 7-AAD (Biolegend). For CP<sup>hi</sup>-BAMs, 14,000–18,000 cells were sorted four independent times. For D<sup>hi</sup>-BAMs and D<sup>lo</sup>-BAMs, 9,000–18,000 and 7,000–15,000 cells, respectively, were sorted four independent times, 30,000 microglia were sorted three independent times and 30,000 peritoneal macrophages and 25,000 alveolar and Kupffer cells were sorted four independent times. Samples were sorted in 500 µl Buffer RLT (Qiagen RNeasy Plus Micro Kit) containing 1% 2-mercaptoethanol (Sigma-Aldrich). Cell sorting was performed using the BD FACS ARIA II. RNA was isolated using the Qiagen RNeasy Plus Micro Kit following the manufacturer’s instructions. RNA concentration and purity were determined spectrophotometrically using the Nanodrop ND-1000 (Nanodrop Technologies), and RNA integrity was assessed using a 2100 Bioanalyzer (Agilent). Per sample, 1 ng of total RNA was used as input for the SMART-Seq v.4 Ultra Low Input RNA protocol (No. 040215) from Clontech Laboratories, Inc. Subsequently, 1 ng of purified cDNA was sheared to 300 bp using Covaris M220. From the sheared material, sequencing libraries were prepared with the NEBNext Ultra DNA Library Prep Kit for Illumina (v.2.0–1/15) according to the manufacturer’s protocol, including an insert size selection of 250 bp. Sequence libraries of each sample were finally equimolarly pooled and sequenced on NextSeq500 flow-cell: high output, 75 bp, single reads, v.2.

**Bulk RNA-seq data analysis.** Preprocessing of the RNA-seq data was done using Trimmomatic. The adapters were cut off, and reads were trimmed when the quality dropped below 20. Reads of length <35 were discarded. All samples passed quality control based on the results of FastQC. Reads were mapped to the mouse reference genome (mm10) via Tophat2 and counted by HTSeqCount. Samples were subsequently analyzed using R/Bioconductor, and the R package limma<sup>62</sup> was used to normalize the data and to perform differential expression analysis. For analysis of differential expression genes, we applied a stringency level where the adjusted *P* value was equal to 0.05 and log<sub>2</sub>FC (where FC is fold change) was less than -1 or >1. A list of core genes for a specific sample or group of samples was generated by first calculating the differential expression genes between the sample(s) of interest and all other samples. This list of differential expression genes was then filtered for those genes showing a mean and median difference >1 between the sample(s) of interest and all other samples. Expression of the resulting genes was then transformed into values between 0 and 1. Only those genes that followed the desired expression profile—for example, normalized expression values <0.5 for all samples, except for the sample(s) of interest where the values should be >0.5—were kept. Finally, we also removed all genes with normalized counts <100.

**Statistics.** All graphs represent mean ± s.e.m. The difference between two means in the phagocytosis assay (Fig. 6h), the germ-free experiment (Fig. 7f) and the PLX3397 depletion and repopulation experiments (Fig. 7i–k and Supplementary Fig. 8) was analyzed using two-tailed unpaired student’s *t*-test in Graphpad Prism v.7.03 and Graphpad Prism v.8.0. The decline in the percentage of YFP<sup>+</sup> cells (Fig. 7c) and the increase in the percentage of YFP<sup>+</sup> cells (Fig. 7d) were evaluated using one-way ANOVA in IBM SPSS Statistics. In Fig. 4d–f, differential expression is assessed using the moderated *t*-statistic (two-sided) and empirical Bayes moderation of the standard errors towards a common value as implemented in the Rbioconductor limma package (eBayes function, default parameters).<sup>62,63</sup> *P* values were corrected for multiple testing by the Benjamini–Hochberg method. In Figs. 6a,d,e and 8g,m and Supplementary Figs. 1c, 2d,g and 11b,d,e, differential expression was assessed using the Wilcoxon rank sum test (two-sided) as implemented in the Seurat R package. *P* value adjustment was performed using Bonferroni correction based on the total number of genes in the dataset. Data distribution was assumed to be normal, but this was not formally tested. Sample sizes were determined through power analysis using G\*Power v.3.0.10. Details of this analysis can be found in the Reporting Summary. Data collection and analysis were not performed blind to the conditions of the experiments.

**Functional analysis using gene ontology enrichment analysis.** To predict putative biological functions based on differentially expressed genes, we carried out a gene ontology enrichment analysis. Genes that were differentially expressed (adjusted *P* < 0.01) between microglia and D<sup>lo</sup>-BAMs, D<sup>hi</sup>-BAMs and CP<sup>hi</sup>-BAMs were used to determine lists of shared and BAM subset-specific genes (see Venn diagram in Fig. 4g). All genes with at least a twofold change in expression (log<sub>2</sub>FC > 1) were selected (CP<sup>hi</sup>-BAM: 129, D<sup>hi</sup>-BAM: 151, D<sup>lo</sup>-BAM: 112, shared CP<sup>hi</sup>-BAM and D<sup>hi</sup>-BAM: 70, shared D<sup>hi</sup>-BAM and D<sup>lo</sup>-BAM: 190) and inserted into BINGO v.3.0.3. (ref. <sup>64</sup>) to obtain enriched ontologies using the standard settings. An enrichment map was produced based on these ontologies using EnrichmentMap v.3.1.0. (ref. <sup>65</sup>) (false discovery rate *q*-value, 0.05, *P* < 0.001, Jaccard 0.25) and AutoAnnotate v.1.2. (ref. <sup>66</sup>) in Cytoscape 3.5.1 (ref. <sup>61</sup>). The color of the nodes represents the BAM subset or shared BAM subset to which they belong. The 385 genes with log<sub>2</sub>FC > 1 and the 432 genes with log<sub>2</sub>FC lower than -1 and that were shared between all BAM subsets were used to produce two additional enrichment maps. The gene ontology enrichment map of the DAM and CP<sup>hi</sup>-BAMs was produced starting from the genes that were differentially expressed between both subsets and microglia (-log<sub>10</sub> *P* adjusted > 10). Genes with log<sub>2</sub>FC > 1 from each subset were selected. CP<sup>hi</sup>-BAM-specific genes (*n* = 235), DAM-specific genes (*n* = 82) and those shared

between these two subsets ( $n=98$ ) were used to produce an enrichment map. The color of the nodes corresponds to the subset.

**Tamoxifen treatment.** Three-to-four-week-old *Cx3cr1<sup>CreER</sup>*:R26-YFP and *Sall1<sup>CreER</sup>*:R26-YFP mice were treated with 4 mg tamoxifen (Sigma-Aldrich) dissolved in 200  $\mu$ l corn oil (Sigma-Aldrich), which was injected subcutaneously near the fore- and hindlimbs (4  $\times$  50  $\mu$ l). These injections were repeated three times at 48 h intervals.

**Immunohistochemistry of brain sections and wholemounts.** Mice were deeply anaesthetized and transcardially perfused with ice-cold PBS followed by 4% ice-cold paraformaldehyde (PFA)/PBS solution. Brains were carefully removed and post-fixed in 4% PFA/PBS at 4°C for 4 h. These were then dehydrated in 15% sucrose/PBS (overnight) followed by 30% sucrose/PBS (overnight), embedded in Tissue-Tek O.C.T compound (Sakura Finetek Europe) and frozen using dry ice. Cryosections (12  $\mu$ m) were made using a Leica CM 1850 UV. Sections were blocked and permeabilized using 0.1% PBS-Triton X-100 (PBS-T, Sigma-Aldrich) containing 10% normal donkey serum (NDS, v/v) (Sigma) for 1 h. Sections were incubated with primary antibodies (diluted in PBS-T solution containing 3% NDS) overnight at 4°C in a moist chamber. The following primary antibodies were used: chicken anti-GFP (No. Ab13970, polyclonal, Lot No. GR3190550-3, Abcam, 1/250), mouse anti-cytokeratin (No. Ab7753, clone C-11, Lot No. GR3190550-3, Abcam, 1/500), rabbit anti-IBA1 (No. 019-19741, polyclonal, Lot No. WDE1198, Wako, 1/500), rat anti-CLEC12A (No. 143402, clone 5D3/Clec12a, Lot No. B151240, BioLegend, 1/100), rat anti-mDectin (CLEC7A) (No. Mabg-mdec, clone R1-8g7, Lot No. MD1-39-01, InvivoGen, 1/30), goat anti-ApoE (No. AB947, polyclonal, Lot No. 3046820, Merck, 5  $\mu$ g ml<sup>-1</sup>). Secondary antibodies were incubated for 1.5 h at room temperature. The following secondary antibodies were used: goat anti-chicken Alexa Fluor 488 (No. A11039, polyclonal, Lot No. 1691381, Life Technologies, 1/500), goat anti-rat Alexa Fluor 555 (No. A21434, polyclonal, Lot No. 1722994, Life Technologies, 1/500), donkey anti-rabbit Alexa Fluor 647 (No. A31573, polyclonal, Lot No. 1693297, Life Technologies, 1/500), goat anti-mouse Alexa Fluor 546 (No. A21123, polyclonal, Lot No. 1830291, Invitrogen, 1/500) and donkey anti-goat Alexa Fluor 568 (No. A11057, polyclonal, Lot No. 1975005, Invitrogen, 1/500). Samples were mounted using mowiol mounting medium (Polysciences, Inc.).

Dura wholemounts were obtained by removing the dura from the skull cap after PFA perfusion. Wholemounts of the enriched SDM were obtained by cutting a thin slice of the dorsal cortex using a 0.25 mm low-profile disposable blade 918 (Leica BioSystems). Wholemounts were post-fixed on ice-cold 4% PFA for 2–2.5 h, after which they were washed with PBS (2  $\times$  3 min) at room temperature. Wholemounts were blocked and permeabilized in 0.1% (dura) or 0.3% (enriched SDM) PBS-T containing 10% NDS (v/v) for 1.5 h. Primary antibodies were diluted in 3% NDS PBS-T solution and left to incubate overnight at 4°C in a moist chamber. The following primary antibodies were used: rat anti-Lyve1 (No. 14-0443-82, clone ALY7, Lot No. 4316105, BD biosciences, 1/100), rat anti-CD31 (No. 550274, clone MEC 13.3, Lot No. 5162734, BD biosciences, 1/100), rabbit anti-IBA1 (No. 019-19741, polyclonal, Lot No. WDE1198, Wako, 1/500) and chicken anti-GFP (No. Ab13970, polyclonal, Lot No. GR3190550-3, Abcam, 1/250). Secondary antibodies were diluted in 3% NDS 0.1% or 0.3% PBS-T solution and incubated for 1.5 h: goat anti-chicken Alexa Fluor 488 (No. A11039, polyclonal, Lot No. 1691381, Life Technologies, 1/500), goat anti-rat Alexa Fluor 555 (No. A21434, polyclonal, Lot No. 1722994, Life Technologies, 1/500) and donkey anti-rabbit Alexa Fluor 647 (No. A31573, polyclonal, Lot No. 1693297, Life Technologies, 1/500). Wholemounts were mounted using mowiol mounting medium. Images were taken using either the Zeiss LSM880 Fast Airy scan or the Zeiss LSM710. Images were analyzed using Fiji<sup>67</sup>.

**Phagocytosis assay.** Single-cell suspensions were prepared from the CP and brain of *Sall1<sup>CreER</sup>*:R26-YFP mice following the above-mentioned procedures. Approximately 2  $\times$  10<sup>5</sup> total brain or CP cells were used per sample and were left on ice for 30 min to slow cell metabolism. Subsequently, cells were resuspended in 100  $\mu$ l pHRodo *Escherichia coli* BioParticles conjugate for phagocytosis (Thermo Fisher) reconstituted in 2 ml per vial of RPMI supplemented with 10% (v/v) heat-inactivated fetal calf serum (Gibco), 300 mg ml<sup>-1</sup> L-glutamine (Gibco), 100 U ml<sup>-1</sup> penicillin and 100 mg ml<sup>-1</sup> streptomycin (Gibco). Cells were incubated for 1.5 h at 37°C to facilitate uptake of particles.

**PLX3397-mediated depletion of brain macrophages.** PLX3397 (Advanced Chemblock, Inc.) was incorporated in AIN-76A chow by Research Diets, Inc. at a concentration of 290 mg kg<sup>-1</sup>. To achieve depletion, C57BL/6, *Cx3cr1<sup>CreER</sup>*:R26-YFP

and *Sall1<sup>CreER</sup>*:R26-YFP mice were given PLX3397 food ad libitum for 21 days. Control mice received AIN-76A standard chow for the same period. To facilitate repopulation, *Cx3cr1<sup>CreER</sup>*:R26-YFP and *Sall1<sup>CreER</sup>*:R26-YFP mice were given AIN-76A standard chow ad libitum for 10 days. Treated and non-treated mice were randomized based on age and sex.

**Reporting Summary.** Further information on research design is available in the Nature Research Reporting Summary linked to this article.

## Data availability

To facilitate the use of our single-cell datasets, an online tool was generated for evaluation of gene expression at single-cell resolution: [www.brainimmuneatlas.org](http://www.brainimmuneatlas.org). All gene-cell count matrices can also be downloaded via this link. In addition, all scRNA-seq and bulk RNA-seq data are also deposited at GEO (NCBI) with accession code GSE128855. Other data that support the findings of this study are available from the corresponding author upon request. There are no restrictions on data availability.

## Code availability

The R codes that were used for scRNA-seq and bulk RNA-seq data analysis can be found at Github: <https://github.com/saeyslab/brainimmuneatlas/>

## References

50. Radde, R. et al. A $\beta$ 42-driven cerebral amyloidosis in transgenic mice reveals early and robust pathology. *EMBO Rep.* **7**, 940–946 (2006).
51. Yona, S. et al. Fate mapping reveals origins and dynamics of monocytes and tissue macrophages under homeostasis. *Immunity* **38**, 79–91 (2013).
52. Benz, C., Martins, V. C., Radtke, F. & Bleul, C. C. The stream of precursors that colonizes the thymus proceeds selectively through the early T lineage precursor stage of T cell development. *J. Exp. Med.* **205**, 1187–1199 (2008).
53. Inoue, S., Inoue, M., Fujimura, S. & Nishinakamura, R. A mouse line expressing *Sall1*-driven inducible cre recombinase in the kidney mesenchyme. *Genesis* **48**, 207–212 (2010).
54. Madisen, L. et al. A robust and high-throughput Cre reporting and characterization. *Nat. Neurosci.* **13**, 133–140 (2010).
55. Lun, A. T. L., McCarthy, D. J. & Marioni, J. C. A step-by-step workflow for low-level analysis of single-cell RNA-seq data with Bioconductor. *F1000Res.* **5**, 2122 (2016).
56. Xu, C. & Su, Z. Identification of cell types from single-cell transcriptomes using a novel clustering method. *Bioinformatics* **31**, 1974–1980 (2015).
57. Levine, J. H. et al. Data-driven phenotypic dissection of AML reveals progenitor-like cells that correlate with prognosis. *Cell* **162**, 184–197 (2015).
58. Satija, R., Farrell, J. A., Gennert, D., Schier, A. F. & Regev, A. Spatial reconstruction of single-cell gene expression data. *Nat. Biotechnol.* **33**, 495–502 (2015).
59. Bray, N. L., Pimentel, H., Melsted, P. & Pachter, L. Near-optimal probabilistic RNA-seq quantification. *Nat. Biotechnol.* **34**, 525–527 (2016).
60. Janky, R. et al. iRegulon: from a gene list to a gene regulatory network using large motif and track collections. *PLoS Comput. Biol.* **10**, e1003731 (2014).
61. Shannon, P. et al. Cytoscape: a software environment for integrated models of biomolecular interaction networks. *Genome Res.* **13**, 2498–2504 (2003).
62. Smyth, G. K. limma: Linear Models for Microarray Data. in *Bioinformatics and Computational Biology Solutions Using R and Bioconductor Ch.23* (eds. Gentleman, R., Carey, V., Huber, W., Irizarry, R. & Dudoit, S.) 397–420 (Springer-Verlag, 2005).
63. Smyth, G. K. Linear models and empirical Bayes methods for assessing differential expression in microarray experiments. *Stat. Appl. Genet. Mol. Biol.* **3**, 1–25 (2004).
64. Maere, S., Heymans, K. & Kuiper, M. BiNGO: a Cytoscape plugin to assess overrepresentation of gene ontology categories in biological networks. *Bioinformatics* **21**, 3448–3449 (2005).
65. Merico, D., Isserlin, R., Stueker, O., Emili, A. & Bader, G. D. Enrichment Map: a network-based method for gene-set enrichment visualization and interpretation. *PLoS One* **5**, e13984 (2010).
66. Kucera, M., Isserlin, R., Arkhangorodsky, A. & Bader, G. D. AutoAnnotate: a Cytoscape app for summarizing networks with semantic annotations. *F1000Res.* **5**, 1717 (2016).
67. Schindelin, J. et al. Fiji: an open-source platform for biological-image analysis. *Nat. Methods* **9**, 676–682 (2012).

# Reporting Summary

Nature Research wishes to improve the reproducibility of the work that we publish. This form provides structure for consistency and transparency in reporting. For further information on Nature Research policies, see [Authors & Referees](#) and the [Editorial Policy Checklist](#).

## Statistics

For all statistical analyses, confirm that the following items are present in the figure legend, table legend, main text, or Methods section.

n/a Confirmed

- The exact sample size ( $n$ ) for each experimental group/condition, given as a discrete number and unit of measurement
- A statement on whether measurements were taken from distinct samples or whether the same sample was measured repeatedly
- The statistical test(s) used AND whether they are one- or two-sided  
*Only common tests should be described solely by name; describe more complex techniques in the Methods section.*
- A description of all covariates tested
- A description of any assumptions or corrections, such as tests of normality and adjustment for multiple comparisons
- A full description of the statistical parameters including central tendency (e.g. means) or other basic estimates (e.g. regression coefficient) AND variation (e.g. standard deviation) or associated estimates of uncertainty (e.g. confidence intervals)
- For null hypothesis testing, the test statistic (e.g.  $F$ ,  $t$ ,  $r$ ) with confidence intervals, effect sizes, degrees of freedom and  $P$  value noted  
*Give P values as exact values whenever suitable.*
- For Bayesian analysis, information on the choice of priors and Markov chain Monte Carlo settings
- For hierarchical and complex designs, identification of the appropriate level for tests and full reporting of outcomes
- Estimates of effect sizes (e.g. Cohen's  $d$ , Pearson's  $r$ ), indicating how they were calculated

*Our web collection on [statistics for biologists](#) contains articles on many of the points above.*

## Software and code

Policy information about [availability of computer code](#)

Data collection

Flow cytometry data was collected using BD FACSDiva version 4.0. and confocal images were collected using ZEN black (Zeiss).

Data analysis

Sequencing data were analyzed using Cell Ranger (10x Genomics), Seurat v2.3.0 and v2.3.4, SCENIC, SCORPIUS, Scater version 1.6.1 and 1.10.0, scran version 1.6.6. and 1.10.1, GENIE3 version 1.0.0. and 1.4.0, limma version 3.34.6, kallisto version v0.45.0, Trimmomatic version v0.3. and R-studio. Gene Ontology Networks were made using cytoscape 3.5.1. and the following cytoscape plugins: Enrichment map v3.1.0., Bingo 3.0.3. AutoAnnotate v1.2. and iRegulon 1.3. Statistics were performed on Graphpad Prism 7.03. and Graphpad Prism 8.0 and IBM SPSS Statistics. Flow cytometry data was analyzed using FlowJo\_V10 and Cytobank.

For manuscripts utilizing custom algorithms or software that are central to the research but not yet described in published literature, software must be made available to editors/reviewers. We strongly encourage code deposition in a community repository (e.g. GitHub). See the Nature Research [guidelines for submitting code & software](#) for further information.

## Data

Policy information about [availability of data](#)

All manuscripts must include a [data availability statement](#). This statement should provide the following information, where applicable:

- Accession codes, unique identifiers, or web links for publicly available datasets
- A list of figures that have associated raw data
- A description of any restrictions on data availability

To facilitate the use of our single-cell datasets an online tool was generated for evaluating gene expression at single-cell resolution: [www.brainimmuneatlas.org](http://www.brainimmuneatlas.org). All gene-cell count matrices can also be downloaded via this link. In addition, all single-cell RNA-seq and bulk RNA-seq raw data are deposited at GEO (NCBI). The data that support the findings of this study are available from the corresponding author upon request. There are no restrictions on data availability.

# Field-specific reporting

Please select the one below that is the best fit for your research. If you are not sure, read the appropriate sections before making your selection.

- Life sciences     Behavioural & social sciences     Ecological, evolutionary & environmental sciences

For a reference copy of the document with all sections, see [nature.com/documents/nr-reporting-summary-flat.pdf](https://nature.com/documents/nr-reporting-summary-flat.pdf)

## Life sciences study design

All studies must disclose on these points even when the disclosure is negative.

### Sample size

Sample sizes for the scRNA sequencing, Bulk RNA sequencing and FACSymphony experiments were determined based what is commonly used for these techniques in the literature. The sample size for the CX3CR1CreERT2 x R26-YFP lineage tracing experiments was determined using power analysis using the following parameters: F-tests: One-way ANOVA, effect size 1.47, a err prob: 0.05, Power: 0.8, number of groups: 5 leading to a total sample size of 15 so 3 mice per timepoint. We used 3-4 mice per timepoint. The sample size for the Flt3Cre x R26-YFP fatemapping experiment was determined using power analysis using the following parameters: F-tests: One-way ANOVA, effect size: 1.20, a errprob: 0.05, Power: 0.8, number of groups: 3 (3W, 6W, 10W) leading to a total sample size of 12 so 4 mice per timepoint. We used 4- 5 mice per timepoint. The sample size for the germ-free experiment was determined using power analysis using the following parameters: t-tests: unpaired, two-sided, effect size d: 2.17, a err prob: 0.05, Power: 0.8 leading to a total sample size of 10 or 5 animals per group. In the conventional and SPF group 10 animals were used and in the germ-free group 4-8 mice. The sample size for the phagocytosis assay was determined using power analysis using the following parameters: t-tests: unpaired, two-sided, effect size d: 4.7, a err prob: 0.05, Power: 0.8 leading to a total sample size of 6 or 3 animals per group. The sample size for the PLX3397 depletion experiment was determined using power analysis using the following parameters: t-tests: unpaired, two-sided, effect size d: 2.8, a err prob: 0.05, Power: 0.8 leading to a total sample size of 8 or 4 animals per group. We used 6 animals per group. The sample size for the repopulation experiments in CX3CR1CreER x R26-YFP mice was determined using power analysis using the following parameters: t-tests: unpaired, two-sided, effect size d: 1.8 , a err prob: 0.05, Power: 0.8 leading to a total sample size of 12 or 6 animals per group. We used 8 animals per group. The sample size for the repopulation experiments in Sall1CreER x R26-YFP mice was determined using power analysis using the following parameters: t-tests: unpaired, two-sided, effect size d: 3.6 , a err prob: 0.05, Power: 0.8 leading to a total sample size of 6 or 3 animals per group. We used 3 control mice and 5 PLX3397-treated mice. Power analyses were performed using G\*Power version 3.0.10.

### Data exclusions

For scRNA-Seq experiments cell filtering was performed as follows: Outlier cells were first identified based on 3 metrics (library size, number of expressed genes and mitochondrial proportion) and cells were tagged as outliers when they were 4 median absolute deviation (MADs) away from the median value of each metric across all cells. Secondly, a PCA plot was generated based on the following metrics: 'pct\_counts\_in\_top\_100\_features', 'total\_features\_by\_counts', 'pct\_counts\_feature\_control', 'total\_features\_by\_counts\_feature\_control', 'log10\_total\_counts\_endogenous' and 'log10\_total\_counts\_feature\_control'. Outlier cells in this PCA plot were identified using the R package mvoutlier. Outside single cell experiments no data was excluded.

### Replication

For WT C57BL/6 experiments we pooled: whole brains from 4 individual mice, enriched subdural meninges and dura from 18 individual mice and choroid plexus (from the lateral and fourth ventricle) from 21 individual mice (9-week-old male). For the scRNA-Seq comparison between our standard and ActD protocol, we pooled: dura and choroid plexus (from the lateral and fourth ventricle) from 10 individual mice for each protocol (9-week-old male C57BL/6). For Irf8-KO experiments we pooled: brains (from which the CP was removed) from 4 CD64Cre/+ x Irf8fl/fl or 4 CD64+/+ x Irf8fl/fl mice and choroid plexus from 7 CD64Cre/+ x Irf8fl/fl or 8 CD64+/+ x Irf8fl/fl mice (7-11-week-old female). For APP/PS1 experiments we pooled whole brains from: 2 individual 9-month-old APP/PS1 mice, 2 16-month-old APP/PS1 mice and 2 16-month-old C57BL/6 non-transgenic controls. The Bulk RNA-seq experiments were repeated four independent times starting from four different sorts per cell type (3 times for microglia). All attempts at replication were successful. FACSymphony experiments were repeated three independent times and all attempts at replication were successful.

### Randomization

Randomization was performed for the PLX3397 depletion and repopulation experiments. C57BL/6 mice were randomly distributed into the control group and the PLX3397-treated group upon arrival to our facility. Sall1CreER/CX3CR1CreER x R26-YFP mice were randomised as much as possible to make sure the PLX3397-treated and control groups had the same amount of males and females and the same amount of mice of each age. No randomization was performed in other experiments as we did not compare mice receiving different treatment in these experiments.

### Blinding

Data collection and analysis were not performed blind to the conditions of the experiments.

## Reporting for specific materials, systems and methods

We require information from authors about some types of materials, experimental systems and methods used in many studies. Here, indicate whether each material, system or method listed is relevant to your study. If you are not sure if a list item applies to your research, read the appropriate section before selecting a response.

## Materials & experimental systems

n/a	Involved in the study
<input type="checkbox"/>	<input checked="" type="checkbox"/> Antibodies
<input checked="" type="checkbox"/>	<input type="checkbox"/> Eukaryotic cell lines
<input checked="" type="checkbox"/>	<input type="checkbox"/> Palaeontology
<input type="checkbox"/>	<input checked="" type="checkbox"/> Animals and other organisms
<input checked="" type="checkbox"/>	<input type="checkbox"/> Human research participants
<input checked="" type="checkbox"/>	<input type="checkbox"/> Clinical data

## Methods

n/a	Involved in the study
<input checked="" type="checkbox"/>	<input type="checkbox"/> ChIP-seq
<input type="checkbox"/>	<input checked="" type="checkbox"/> Flow cytometry
<input checked="" type="checkbox"/>	<input type="checkbox"/> MRI-based neuroimaging

## Antibodies

### Antibodies used

Flow cytometry  
 Antigen/ Fluorophore /Dilution/ Clone /Lot number /ID /Manufacturer  
 Armenian Hamster IgG1 Isotype Ctrl/FITC/1:300/ HTK888/ B208511/ 400906/ BioLegend  
 CD11a/ BV786/ 1:300/ M17/4/ 8298571/ 740866/ BDbiosciences  
 CD11a/ Pe/ 1:300/ M17/4/ E01070-82/ 12-0111-82/ eBioScience  
 CD11b/ BUV737/ 1:300/ M1/70/ 8081887/ 564443/ BDbiosciences  
 CD11b1/ PE/cy7/ 1:300/ M1/7/ B227804/ 101216/ Biolegend  
 CD11c/ PE/cy5/ 1:300/ N418/ B195382/ 117316/ Biolegend  
 CD204 (MSR1)/ PE/ 1: 300/ M204PA/ 4325850/ 12-2046-86/ eBioScience  
 CD206 (MMR)/ AF647/ 1:300/ C068C2/ B230155/ 141711/ BioLegend  
 CD206 (MMR)/ FITC/ 1:300/ C068C2/ B213957/ 141704/ BioLegend  
 CD301 (CLEC10a)/ PE/ 1:300/ LOM-14/ B198443/ 145703/ BioLegend  
 CD304 (NRP1)/ BV421/ 1:300/ 3E12/ B246181/ 145209/ BioLegend  
 CD304 (NRP1)/ PE/ 1:300/ 3E12/ B226496/ 145203/ BioLegend  
 CD36/ PE/ 1:300/ HM36/ B223035/ 102605/ BioLegend  
 CD371 (CLEC12A)/ Pe/ 1:300/ 5D3/ B211136/ 143403/ BioLegend  
 CD371 (CLEC12A)/ APC/ 1:300/ 5D3/ B188838/ 143405/ BioLegend  
 CD41/ BUV805/ GK1.5/ 1:300/ 7125755/ 564922/ BD Horizon  
 CD43/ BUV737/ S7/ 1:300/ 7143811/ 564398/ BD Horizon  
 CD44/ BV570/ IM7/ 1:300/ B237222/ 103037/ BioLegend  
 CD45/ APC/cy7/ 1:300/ 30-F11/ B242535/ 103115/ Biolegend  
 CD45/ BV421/ 1:300/ 30-F11/ B232006/ 103133/ BioLegend  
 CD45/ BUV661/ 1:300/ 30-F11/ 7207676/ 565079/ BD Horizon  
 CD45R/B220/ BUV496/ 1:300/ RA3-6B2/ 7018902/ 564662/ BD Horizon  
 CD54 (ICAM-1)/ PE/ 1:300/ YN1/1.7.4/ B259665/ 116107/ BioLegend  
 CD63/ PE/Dazzle™ 594/ 1:300/ NVG-2/ B230296/ 143913/ BioLegend  
 CD63/ PE/ 1:300/ NVG-2/ B209580/ 143903/ BioLegend  
 CD64/ BV605/ 1:300/ X54-5/7.1/ B240410/ 139323/ BioLegend  
 CD8a/ APC/cy7/ 1:300/ 53-6.7/ B217171/ 100713/ BioLegend  
 c-MAF/ PE/ 1:30/ Sym0F1/ 4336580/ 12-9855-41/ eBioScience  
 CX3CR1/ APC/ 1:300/ SA011F11/ B200994/ 149007/ BioLegend  
 CX3CR1/ Pe/ 1:300/ SA011F11/ B194103/ 149005/ BioLegend  
 CX3CR1/ Alexa Fluor 700/ 1:300/ SA011F11/ B264652/ 149035/ Biolegend  
 CX3CR1/ BV421/ 1:300/ SA011F11/ B231871/ 149023/ Biolegend  
 F4/80/ BV650/ 1:300/ BM8/ B256505/ 123149/ BioLegend  
 F4/80/ PE-CF594/ 1:300/ T45-2342/ 7241543/ 565613/ BD Horizon  
 Folate Receptor  $\beta$  (FR- $\beta$ )/ 1:300/ PE/ 10/FR2/ B248263/ 153303/ BioLegend  
 I-A/I-E/ PerCP/cy5.5/ 1:300/ M5/114.15.2/ B253463/ 107602/ Biolegend  
 IRF7/ PE/ 1:30/ MNGPKL/ 1997022/ 12-9855-41/ eBioScience  
 IRF8/ PE/ 1:30/ V3GYWCH/ 4318614/ 12-9852-80/ eBioScience  
 Ly6C/ APC/Fire™ 750/ 1:300/ HK1.4/ B261781/ 128045/ BioLegend  
 Ly-6C/ AF647/ 1:300/ ER-MP20/ 1113/ MCA2389A647/ BioRAD  
 Ly-6C/ FITC/ 1:300/ AL-21/ 4024747/ 553104/ BD Biosciences  
 Ly-6C/ BV785/ 1:300/ HK1.4/ B237063/ 128041/ BioLegend  
 Ly-6G/ Pe/ 1:300/ 1A8/ B221647/ 127607/ Biolegend  
 Ly6G/ BUV563/ 1:300/ 1A8/ 7097851/ 565707/ BD Horizon  
 MERTK/ PE/ 1:300/ 2B10C42/ B235411/ 151506/ BioLegend  
 P2RX7/ PE/cy7/ 1:300/ 1F11/ B247119/ 148707/ BioLegend  
 P2RX7/ PE/ 1:300/ 1F11/ B233103/ 148703/ BioLegend  
 Rat IgG2a,  $\kappa$  Isotype Ctrl/ PE/ 1:300/ MOPC-173/ B250383/ 400214/ BioLegend  
 XCR1/ BV650/ 1:300/ ZET/ B241219/ 148220/ BioLegend

### IHC

chicken anti-GFP (id. Ab13970, polyclonal, lotnr. GR3190550-3, Abcam, 1/250)  
 mouse anti-cytokeratin (id. Ab7753, clone C-11, lotnr. GR3190550-3, Abcam, 1/500)  
 rabbit anti-IBA1 (id. 019-19741, polyclonal, lotnr. WDE1198, Wacko, 1/500)  
 rat anti-CLEC12A (id. 143402, clone 5D3/Clec12a, lotnr. B151240, BioLegend, 1/100)  
 rat anti-mDectin (CLEC7A) (id. Mabg-mdect, clone R1-8g7, lotnr. MD1-39-01, InvivoGen, 1/30)

## Validation

goat anti-ApoE (id. AB947, polyclonal, lotnr. 3046820, Merck, 5µg/ml)  
 Goat anti-chicken Alexa Fluor 488 (id. A11039, polyclonal, lotnr. 1691381, Life Technologies, 1/500)  
 Goat anti-rat Alexa Fluor 555 (id. A21434, polyclonal, lotnr. 1722994, Life Technologies, 1/500)  
 Donkey anti-rabbit Alexa Fluor 647 (id. A31573, polyclonal, lotnr. 1693297, Life Technologies, 1/500)  
 Goat anti-mouse Alexa Fluor 546 (id. A21123, polyclonal, lotnr. 1830291, Invitrogen, 1/500)  
 Donkey anti-goat Alexa Fluor 568 (id A11057, polyclonal, lotnr. 1975005, Invitrogen, 1/500)

Flow cytometry:  
 CD206-FITC: <https://www.biolegend.com/fr-fr/products/fitc-anti-mouse-cd206-mmr-antibody-7318>. doi:10.1016/j.bbrc.2011.11.088  
 CD371(Clec12a)-APC: <https://www.biolegend.com/fr-fr/products/apc-anti-mouse-cd371-clec12a-antibody-10322>.  
 CD24-AF700: <https://www.biolegend.com/fr-fr/products/alexa-fluor-700-anti-mouse-cd24-antibody-12790>. doi: 10.4049/jimmunol.0900062  
 CD8a-APC/cy7: <https://www.biolegend.com/fr-fr/products/apc-cy7-anti-mouse-cd8a-antibody-2269>. doi: 10.1093/intimm/dxh340  
 CD44-BV570: <https://www.biolegend.com/fr-fr/products/brilliant-violet-570-anti-mouse-human-cd44-antibody-7386>. doi: 10.1186/1479-5876-7-89  
 CD64-BV605: <https://www.biolegend.com/fr-fr/products/brilliant-violet-605-anti-mouse-cd64-fcgammari-antibody-13611>. doi: 10.1182/blood-2009-07-235028  
 Xcr1-BV650: <https://www.biolegend.com/fr-fr/products/brilliant-violet-650-anti-mouse-rat-xcr1-antibody-12421>. doi: 10.3389/fimmu.2015.00035  
 Ly-6C-BV785: <https://www.biolegend.com/fr-fr/products/brilliant-violet-785-anti-mouse-ly-6c-antibody-11982>. doi: 10.1101/gad.1771409  
 CD45R/B220-BUV496: <https://www.bdbiosciences.com/us/reagents/research/antibodies-buffers/immunology-reagents/antimouse-cell-surface-antigens/buv496-rat-anti-mouse-cd45rb220-ra3-6b2/p/564662>. doi: <https://doi.org/10.4049/jimmunol.167.3.1393>  
 Ly-6G-BUV563: <http://www.bdbiosciences.com/eu/reagents/research/antibodies-buffers/immunology-reagents/anti-mouseantibodies/cell-surface-antigens/buv563-rat-anti-mouse-ly-6g-1a8/p/565707>. PMID: 8051400.  
 CD45-BUV661: <https://www.bdbiosciences.com/us/applications/research/stem-cell-research/cancer-research/mouse/buv661-rat-anti-mouse-cd45-30-f11/p/565079>. doi: 10.1172/JCI7811  
 CD43-BUV737: <https://www.bdbiosciences.com/us/reagents/research/antibodies-buffers/immunology-reagents/anti-mouseantibodies/cell-surface-antigens/buv737-rat-anti-mouse-cd43-s7/p/564398>. PMID: 9645617  
 CD4-BUV805: <https://www.bdbiosciences.com/us/reagents/research/antibodies-buffers/immunology-reagents/anti-mouseantibodies/cell-surface-antigens/buv805-rat-anti-mouse-cd4-gk15/p/564922>. PMID: 10562325.  
 F4/80-PE-CF594: <https://www.bdbiosciences.com/us/reagents/research/antibodies-buffers/immunology-reagents/anti-mouseantibodies/cell-surface-antigens/pe-cf594-rat-anti-mouse-f480-t45-2342/p/565613>. doi: 10.1007/s11011-015-9714-9.  
 CD11c-PE/cy5: <https://www.biolegend.com/en-us/products/pe-cy5-anti-mouse-cd11c-antibody-3085>. PMID: 16818746.  
 CX3CR1-BV421: <https://www.biolegend.com/en-us/products/brilliant-violet-421-anti-mouse-cx3cr1-antibody-11852>. doi: 10.1016/j.cell.2017.01.006.  
 CD11b-PE/cy7: <https://www.biolegend.com/en-us/products/pe-cy7-anti-mouse-human-cd11b-antibody-1921>. PMID: 16493044.  
 I-A/I-E-PerCP/cy5.5: <https://www.biolegend.com/en-us/products/percp-cy5-5-anti-mouse-i-a-i-e-antibody-4282>. doi: <https://doi.org/10.3389/fimmu.2017.00623>.  
 CD11a-Pe: <https://www.thermofisher.com/antibody/product/CD11a-LFA-1alpha-Antibody-clone-M17-4-Monoclonal/12-0111-82>. doi: 10.1038/cr.2015.61.  
 Ly-6C-AF647: <https://www.bio-rad-antibodies.com/monoclonal/mouse-ly-6c-antibody-er-mp20-mca2389.html?f=alexa%20fluor%C2%AE%20647>. doi: 10.1128/AI.00094-10.  
 Ly-6G-Pe: <https://www.biolegend.com/en-us/products/pe-anti-mouse-ly-6g-antibody-4777>. PMID: 8360469.  
 CD45-APC/cy7: <https://www.biolegend.com/en-us/products/apc-cy7-anti-mouse-cd45-antibody-2530>. PMID: 17911595.  
 Ly-6C-FITC: <https://www.bdbiosciences.com/eu/reagents/research/antibodies-buffers/immunology-reagents/anti-mouseantibodies/cell-surface-antigens/fitc-rat-anti-mouse-ly-6c-al-21/p/553104>. doi: 10.1002/eji.1830181125.  
 CD45-BV421: <https://www.biolegend.com/en-us/products/brilliant-violet-421-anti-mouse-cd45-antibody-7253>. doi: 10.1038/cddis.2016.264.  
 CD206-AF647: <https://www.biolegend.com/en-us/products/alexa-fluor-647-anti-mouse-cd206-mmr-antibody-7427>. doi: 10.1371/journal.pone.0167307.  
 CX3CR1-APC: <https://www.biolegend.com/en-us/products/apc-anti-mouse-cx3cr1-antibody-10460>. doi: 10.1038/mi.2016.139.  
 CX3CR1-PE: <https://www.biolegend.com/en-us/products/pe-anti-mouse-cx3cr1-antibody-10376>. doi: 10.1371/journal.pone.0163607.  
 CD371(Clec12a)-PE: <https://www.biolegend.com/en-us/products/pe-anti-mouse-cd371-clec12a-antibody-7686>.  
 NRP1-BV421: <https://www.biolegend.com/de-de/search-results/brilliant-violet-421-anti-mouse-cd304-neuropilin-1-antibody-8731>. doi: 10.1371/journal.pone.0108023.  
 NRP1-PE: <https://www.biolegend.com/de-de/products/pe-anti-mouse-cd304-neuropilin-1-antibody-8435>. doi: 10.1371/journal.pone.0108023.  
 F4/80-BV650: <https://www.biolegend.com/de-de/products/brilliant-violet-650-anti-mouse-f4-80-antibody-10630>. doi: 10.4049/jimmunol.1202884.  
 CD11a-BV786: <http://www.bdbiosciences.com/us/reagents/research/antibodies-buffers/immunology-reagents/anti-mouseantibodies/cell-surface-antigens/bv786-rat-anti-mouse-cd11a-m174/p/740866>. PMID: 8975879.  
 CX3CR1-AF700: <https://www.biolegend.com/de-de/products/alexa-fluor-700-anti-mouse-cx3cr1-antibody-13474>

Ly6C-APC/Fire™ 750: <https://www.biologegend.com/de-de/products/apc-fire-750-anti-mouse-ly-6c-antibody-13338>. doi: 10.1101/gad.1771409.

FR-β-PE: <https://www.biologegend.com/de-de/products/pe-anti-mouse-folate-receptor-beta-fr-beta-antibody-15147>. doi: 10.1002/art.21228.

CD63-PE/Dazzle™ 594: <https://www.biologegend.com/de-de/products/pe-dazzle-594-anti-mouse-cd63-antibody-11709>.

P2RX7-PE/cy7: <https://www.biologegend.com/de-de/products/pecy7-anti-mouse-p2x7r-antibody-15047>. doi: <https://doi.org/10.1038/ncomms2023>.

CD11b-BUV737: <http://www.bdbiosciences.com/us/applications/research/b-cell-research/surface-markers/mouse/buv737>-ratanti-

CD11b-m170/p/564443. doi: <https://doi.org/10.4049/jimmunol.167.3.1393>.

IRF8-PE: <https://www.thermofisher.com/antibody/product/IRF8-Antibody-clone-V3GYWCH-Monoclonal/12-9852-82>. doi: 10.1016/j.jimmuni.2016.08.015.

IRF7-PE: <https://www.thermofisher.com/antibody/product/IRF7-Antibody-clone-MNGPKL-Monoclonal/12-5829-80>.

c-MAF-PE: <https://www.thermofisher.com/antibody/product/c-MAF-Antibody-clone-sym0F1-Monoclonal/12-9855-41>. doi: 10.1016/j.jimmuni.2013.08.031.

IHC:

- chicken anti-GFP: <http://www.abcam.com/gfp-antibody-ab13970.html>. doi: 10.1038/s41467-017-02785-6.
- rat anti-CD31: <http://www.bdbiosciences.com/us/applications/research/stem-cell-research/cancer-research/mouse/purified-ratanti-mouse-cd31-mec-133/p/550274>. PMID: 9284815.
- mouse anti-cytokeratin: <http://www.abcam.com/pan-cytokeratin-antibody-c-11-ab7753.html>, doi: 10.1038/s41598-018-24825-x.
- rabbit anti-lba: <http://www.wako-chem.co.jp/english/labchem/product/life/Antilba1/index.htm>. doi: <https://doi.org/10.1523/JNEUROSCI.1498-12.2012>.
- rat anti-CD371(Clec12a): <https://www.biologegend.com/de-at/products/purified-anti-mouse-cd371-clec12a-antibody-7685>.
- rat anti-Lyve1: <https://www.thermofisher.com/antibody/product/LYVE1-Antibody-clone-ALY7-Monoclonal/14-0443-80>. doi: 10.1182/blood-2004-08-3382.
- goat anti-Apoe: [http://www.merckmillipore.com/BE/fr/product/Anti-Apolipoprotein-E-Antibody,MM\\_NF-AB947?ReferrerURL=https%3A%2F%2Fwww.google.com%2F&bd=1](http://www.merckmillipore.com/BE/fr/product/Anti-Apolipoprotein-E-Antibody,MM_NF-AB947?ReferrerURL=https%3A%2F%2Fwww.google.com%2F&bd=1). doi: 10.1016/j.jimmuni.2017.08.008.
- Arat anti-mDectin-1 (CLEC7A): <https://www.invivogen.com/anti-mdectin1>. doi: <https://www.invivogen.com/anti-mdectin1>.
- Goat anti-Chicken IgY (H+L) Secondary Antibody, Alexa Fluor 488: <https://www.thermofisher.com/antibody/product/Goat-anti-Chicken-IgY-H-L-Secondary-Antibody-Polyclonal/A-11039>.
- Goat anti-Rat IgG (H+L) Cross-Adsorbed Secondary Antibody, Alexa Fluor 555: <https://www.thermofisher.com/antibody/product/Goat-anti-Rat-IgG-H-L-Cross-Adsorbed-Secondary-Antibody-Polyclonal/A-21434>.
- Donkey anti-Rabbit IgG (H+L) Highly Cross-Adsorbed Secondary Antibody, Alexa Fluor 647: <https://www.thermofisher.com/antibody/product/Donkey-anti-Rabbit-IgG-H-L-Highly-Cross-Adsorbed-Secondary-Antibody-Polyclonal/A-31573>.
- Goat anti-Mouse IgG1 Cross-Adsorbed Secondary Antibody, Alexa Fluor 546: <https://www.thermofisher.com/antibody/product/Goat-anti-Mouse-IgG1-Cross-Adsorbed-Secondary-Antibody-Polyclonal/A-21123>.
- Donkey anti-Goat IgG (H+L) Cross-Adsorbed Secondary Antibody, Alexa Fluor 568: <https://www.thermofisher.com/antibody/product/Donkey-anti-Goat-IgG-H-L-Cross-Adsorbed-Secondary-Antibody-Polyclonal/A-11057>.

## Animals and other organisms

Policy information about [studies involving animals](#); [ARRIVE guidelines](#) recommended for reporting animal research

### Laboratory animals

For scRNA-Seq experiments the following mice were used:

- 1) C57BL/6, Male, 9 weeks
- 2) APP/PS1, Male, 9 or 16 months and corresponding non-transgenic, male, 16 month-old control animals
- 3) CD64Cre/+ × Irf8fl/fl and CD64+/+ × Irf8fl/fl littermates, Female, 7-11 weeks

For Bulk RNA-Seq experiments the following mice were used:

- 1) C57BL/6, Male, 7 weeks

For FACSsymphony experiments the following mice were used:

- 1) C57BL/6, Male, 9 weeks

For flow cytometry the following mice were used:

- 1) Sall1CreER x R26-YFP, Male/Female, 7-10 weeks (Fig. 5 a-c)
- 2) Sall1CreER x R26-YFP, Male/Female, 9-15 weeks (Fig. 6 g-h)
- 3) C57BL/6, Male/Female, PDO, PD8, 2/3/6/20/50 weeks (Fig. 7a-b)
- 4) CX3CR1CreER x R26-YFP, Male/Female, 8-37 weeks (Fig. 7c)
- 5) Flt3Cre x R26-YFP, Male, PDO, PD3, PD6, 3/6/10 weeks (Fig. 7d)
- 6) C57BL/6 Germ-Free, SPF, conventional animal facility, Male/Female, 10 Weeks (Fig 7f)
- 7) C57BL/6, Male, 12 Weeks (Fig 7 h-i + Fig. S8a)
- 8) CX3CR1CreER x R26-YFP, Male/Female, 12-14 Weeks (Fig. 7j + Fig. S8b-d)
- 9) Sall1CreER x R26-YFP, Male/Female, 11-14 weeks (Fig. 7k + Fig. S8e-f)
- 10) C57BL/6, Male, 20 weeks (Fig. S3d)
- 11) C57BL/6, Male, 9 weeks (Fig. S4b)

For Immunohistochemistry the following mice were used:

- 1) CX3CR1CreER x R26-YFP, Male/Female, 8-12 weeks (Fig 3 h-j)
- 2) Sall1CreER x R26-YFP, Male/Female, 7 weeks (Fig. 5 e-f)
- 3) Lyz2-GFP, Male/Female, 7-9 weeks (Fig. 5 g)
- 4) Flt3Cre x R26-YFP, Male, 6-8 weeks (Fig. 7e)
- 5) Sall1CreER x R26-YFP, Male/Female, 7-16 weeks (Fig. S6)

### Wild animals

The study did not involve the use of wild animals.

Field-collected samples

The study did not involve samples collected from the field.

Ethics oversight

All experiments were approved by the Ethische Commissie Dierproeven at the Vrije Universiteit Brussel.

Note that full information on the approval of the study protocol must also be provided in the manuscript.

## Flow Cytometry

### Plots

Confirm that:

- The axis labels state the marker and fluorochrome used (e.g. CD4-FITC).
- The axis scales are clearly visible. Include numbers along axes only for bottom left plot of group (a 'group' is an analysis of identical markers).
- All plots are contour plots with outliers or pseudocolor plots.
- A numerical value for number of cells or percentage (with statistics) is provided.

### Methodology

#### Sample preparation

Mice were deeply anaesthetized and perfused transcardially with 30 ml of ice-cold PBS. For whole brain isolations, mice were decapitated, and brains were placed on ice-cold RPMI (Gibco). Brains were cut into small pieces and enzyme mix (30 U.ml<sup>-1</sup> DNase I (Roche), 10 U.ml<sup>-1</sup> collagenase type I (Worthington) and 400 U.ml<sup>-1</sup> collagenase type IV (Worthington) diluted in 1X HBSS (Gibco)) was added. Following 20 min at 37°C, tissue was crushed with a syringe plunger and homogenized via trituration using standard Serological Pipettes. The solution was filtered twice over a 100µm nylon filter and centrifuged. The pellet was resuspended in 5 ml 70% Standard Isotonic Percoll (SIP) (GE Healthcare) diluted in 1X HBSS and gently overlaid with 5 ml of 37% SIP, followed by a 5 ml layer of 30% SIP, forming a 3-layered density gradient (centrifuged at 800 g, 4°C, 30 min without acceleration/breaks). The 70/37% interphase containing immune cells was collected, centrifuged and resuspended in FACS buffer (2mM EDTA (Duchefa), 2% heat-inactivated fetal calf serum (Gibco) dissolved in 1X HBSS). The dissociation process took 4 hours.

For isolation of the dura mater, the dorsal part of the skull was carefully removed. The dura was peeled off from the skull cap and placed in ice-cold RPMI. The enriched subdural meninges was isolated by manually cutting a thin slice of the dorsal cortex using a 0.25 mm low-profile disposable blade 918 (Leica BioSystems). The slice comprised the area between bregma coordinates 2 mm and -4 mm and was <1 mm thick, weighing ± 5 mg. For isolation of the choroid plexi, the ventricles were exposed after which the choroid plexus of the lateral and the fourth ventricle were carefully micro-dissected and placed in ice-cold RPMI. The choroid plexus, dura and enriched subdural meninges were cut into small pieces and incubated with enzyme mix at 37°C for 30 minutes (the solution was resuspended every 10 minutes). Next, solutions were filtered and centrifuged. Cells from the dura and choroid plexus were resuspended in FACS buffer. To remove myelin, cells from the enriched subdural meninges were resuspended in 30% SIP and centrifuged (800 g, 4°C, 30 min, no acceleration/breaks) and the pellet was resuspended in FACS buffer. The dissociation process took 2 hours and 15 minutes for the dura and choroid plexus and 3 hours for the subdural meninges.

To assess for and limit the induction of dissociation-induced gene expression, we adjusted the protocol described above with ActD modifications. For the ActD isolation protocol the choroid plexus and dura were dissected as mentioned above and placed in ice-cold RPMI containing 30 µM Actinomycin D (Sigma, cat n° A1410). The CP and Dura were cut into small pieces and incubated with enzyme mix containing 15 µM ActD at 11°C for 50 min. Every ten minutes the solution was cut and resuspended in order to ensure full dissociation of the tissue. The remaining process was performed as stated previously with ActD added in 3 steps. Filtering was performed with RPMI, containing 3 µM ActD. The pellet was resuspended in FACS buffer, containing 3 µM ActD and sorted cells were collected in ME medium (RMPI medium supplemented with 20% heat-inactivated fetal calf serum (Gibco), 300 µg/ml-1 L-glutamine (Gibco), 100 units ml-1 penicillin and 100 µg ml-1 streptomycin (Gibco), 1 mM Non-essential amino acids (Gibco), 1 mM sodium pyruvate (Gibco) and 0.05 mM 2-mercapto ethanol (Sigma)), containing 3 µM ActD. The dissociation process took 2 hours and 15 minutes. Cells were kept on ice during all steps, except for the enzymatic digestion. Samples that were processed using ActD were compared to samples processed using the standard protocol, as described above.

#### Instrument

For FACSymphony experiments, the BD FACSymphony(TM) A5 was used. The remaining flow cytometry data was collected using BD FACS Canto(TM) II. Cell sorting was performed on the BD FACS ARIA(TM) II and the BD FACS ARIA(TM) III.

#### Software

Data were collected using the BD FACSDiva(TM) software. The flow cytometry was analysed using FlowJo V10 and Cytobank software (<https://premium.cytobank.org/cytobank/login>).

#### Cell population abundance

The purity of sorted cell fractions was >90% in all experiments.

#### Gating strategy

The gating strategy for the all the different population is described (see Fig. 3 and Supplementary Fig. 3).

Tick this box to confirm that a figure exemplifying the gating strategy is provided in the Supplementary Information.